Article

Nutrient-delivery and metabolism reactivation therapy for melanoma

🔴 Check for updates

Yang Chen [1,2,7], Chaochao Wang[1,2,7], Yelin Wu[1,7], Ya Wang[2], Yun Meng[1], Fan Wu[2], Huilin Zhang[2,3], Yuen Yee Cheng[4], Xingwu Jiang [2], Jieyun Shi[1], Huiyan Li[2], Peiran Zhao[2], Jinfeng Wu [3] ✉, Bin Zheng [5], Dayong Jin [4,6] ✉ & Wenbo Bu [1,2,3] ✉

To fulfil the demands of rapid proliferation, tumour cells undergo significant metabolic alterations. Suppression of hyperactivated metabolism has been proven to counteract tumour growth. However, whether the reactivation of downregulated metabolic pathways has therapeutic effects remains unexplored. Here we report a nutrient-based metabolic reactivation strategy for effective melanoma treatment. L-Tyrosine–oleylamine nanomicelles (MTyr–OANPs) were constructed for targeted supplementation of tyrosine to reactivate melanogenesis in melanoma cells. We found that reactivation of melanogenesis using MTyr–OANPs significantly impeded the proliferation of melanoma cells, primarily through the inhibition of glycolysis. Furthermore, leveraging melanin as a natural photothermal reagent for photothermal therapy, we demonstrated the complete eradication of tumours in B16F10 melanoma-bearing mice through treatment with MTyr–OANPs and photothermal therapy. Our strategy for metabolism activation-based tumour treatment suggests specific nutrients as potent activators of metabolic pathways.

It is well known that tumour cells exhibit a metabolic phenotype quite different to that of healthy cells to meet the requirements of uncontrolled cell proliferation[1,2]. While some metabolic pathways, including glycolysis[3], pentose phosphate pathway[4] and fatty acid synthesis[5], are hyperactivated, some pathways, such as the tricarboxylic acid cycle[6,7], are suppressed. So far, most cancer metabolic therapies have been focused on inhibiting hyperactivated metabolic pathways. For example, the anti-glycolysis drugs lonidamine[8,9] and shikonin[10] have been clinically used for treating various cancers, and aromatase inhibitors that suppress the hyperactive oestrogen synthesis pathway exerts a therapeutic effect on patients with breast cancer[11,12].

The majority of suppressed metabolic pathways in tumours are cell-type specific, and their specialized functions might be unnecessary for tumour proliferation[13–15]. For example, gluconeogenesis is decreased or absent in liver cancer compared with normal liver cells[16,17], and melanogenesis is significantly downregulated in melanomas compared with melanocytes[18–20]. Moreover, antagonistic effects have been reported between cell-type-specific metabolic and cell proliferation pathways[13,14,18,21]. For example, promoting gluconeogenesis in liver and kidney cancer has been reported to decrease the amount of glucose transformed into biosynthetic precursors for the growth of new cells[17,22], and increasing citrate production and secretion in prostate cancer has been found to inhibit the process of citrate oxidation for ATP production, thus influencing prostate cancer growth[23,24].

To activate a signal pathway, the common approach is to screen for activators of key enzymes, which is usually time-consuming and

[1]Department of Medical Ultrasound, Shanghai Tenth People's Hospital, Tongji University Cancer Center, School of Life Sciences and Technology, Tongji University, Shanghai, P. R. China. [2]Department of Materials Science and State Key Laboratory of Molecular Engineering of Polymers, Academy for Engineering and Technology, Fudan University, Shanghai, P. R. China. [3]Department of Dermatology, Huashan Hospital, Fudan University, Shanghai, P. R. China. [4]Institute for Biomedical Materials and Devices (IBMD), Faculty of Science, University of Technology Sydney, Sydney, New South Wales, Australia. [5]Cedars-Sinai Cancer Institute, Department of Biomedical Sciences, Cedars-Sinai Medical Center, Los Angeles, CA, USA. [6]Eastern Institute for Advanced Study, Eastern Institute of Technology, Ningbo, P. R. China. [7]These authors contributed equally: Yang Chen, Chaochao Wang, Yelin Wu. ✉e-mail: jinfengwu@fudan.edu.cn; dayong.Jin@uts.edu.au; wbbu@fudan.edu.cn

expensive, and enzyme activators usually have low bioavailability[25–27]. Apart from this, specific nutrients, such as amino acids[28,29] and fatty acids[30], have been reported to serve as activators of specific metabolic pathways. Nutrients are safe and easy to acquire[31,32], but the low targeting efficiency[33] and insufficient intake of free nutrients by cancer cells[34,35] are the limiting factors towards any practical applications.

In this Article, we propose a nutrient-based metabolism reactivation strategy for tumour treatment. This strategy requires two steps, choosing a suppressed metabolism of a specific tumour, and then using nanotechnology to encapsulate nutrients into biocompatible micelles to reach the high delivery efficiency. Our work here specifically targets the treatment of skin cutaneous melanoma (SKCM). First, using single-sample gene set enrichment analysis (ssGSEA) of the gene signature from The Cancer Genome Atlas (TCGA) in patients with SKCM primary tumours and metastasis, we found a significant downregulation of the gene signature 'KEGG MELANOGENESIS' in metastatic SKCM (Fig. 1a), and patients with SKCM with a low ssGSEA score were found to be correlated with worse 5-year survival outcomes, compared with the high-score group (Fig. 1b). These results showed that melanogenesis metabolism is suppressed in advanced SKCM. Then, we supplemented L-tyrosine (Tyr) using a Tyr-based degradable nanosized micelle (MTyr–OANPs) to restore melanogenesis for melanoma treatment (Fig. 1c) and found that a large amount of Tyr released from MTyr–OANPs intracellularly could reactivate the melanin synthesis. During melanogenesis activation, the reduced glycolysis caused by melanin intermediates arrests the cell cycle. Furthermore, on the basis of the excellent photothermal conversion performance of endogenously produced melanin[36–38], photothermal therapy (PTT) was applied to these MTyr–OANP-treated cells for one-two-punch treatment.

MTyr–OA nanomicelles to enhance tyrosine supplement

The amphipathic MTyr4–OA molecule was synthesized by amidation between MTyr4 and oleylamine, consisting of hydrophilic mannose (M), Tyr4 (short peptide composed of four L-tyrosine) and hydrophobic oleylamine (OA). The MTyr4–OA construct was confirmed by its mass spectrum and ^{1}H NMR spectrum (Fig. 2a,b). Owing to the amphipathic nature of MTyr4–OA, it was easily made into nanomicelles (named MTyr–OANPs). MTyr–OANPs were approximately 60 nm (Fig. 2c), with excellent dispersibility and a narrow particle size distribution (polydispersity index = 0.160) (Supplementary Fig. 1). The zeta potential of MTyr–OANPs was as high as +40.39 mV (Supplementary Fig. 2) to facilitate the efficient uptake by cells. The critical micelle concentration (CMC) of MTyr4–OA was measured as 0.00828 mg ml^{-1} (Fig. 2d). MTyr–OANPs could release L-Tyr monomers when co-treated with peptidase (Fig. 2e,f), indicating that the L-Tyr in MTyr–OANPs could be utilized in a physiological environment.

MTyr–OANPs had favourable stability, as their size distributions remained unchanged at room temperature for half a month (Supplementary Fig. 3). Furthermore, owing to their amphiphilic characteristic and positive charge, MTyr–OANPs could be endocytosed by cells after only 2 h and lasted for 12 h (Fig. 2g). Cells cultured with MTyr–OANPs showed more intracellular L-Tyr than cells cultured with free L-Tyr with the same concentration (Fig. 2h and Supplementary Fig. 4). MTyr–OANPs showed great biocompatibility with normal cells in vitro even at a concentration of up to 1.0 mg ml^{-1} (Supplementary Fig. 5) and no negative effect on the health or weight of the mice over time, examined at a dose of 100 mg kg^{-1} (Supplementary Figs. 6–9).

MTyr–OANPs promoted melanogenesis and arrested cell cycle

As shown in Fig. 3a, the cells were marked with pigmentation after MTyr–OANPs treatment. The melanin content quantified in MTyr–OANP-treated cells after 72 h of incubation was found to increase by six-fold, compared with that in controls, and threefold, compared with that

in free L-Tyr-treated cells (Fig. 3b). The amount of melanosomes where melanin was synthesized (Fig. 3c) and activity of the key rate-limiting enzyme in melanogenesis, tyrosinase, was also found increased (Fig. 3d) after MTyr–OANP treatment. Moreover, melanogenesis-related genes, including *Tyr*, *Tyrp1*, *Tyrp2* and *Mitf*, were all upregulated (Fig. 3e). These results indicate that L-Tyr supplement through MTyr–OANPs activates melanogenesis through increasing tyrosinase activity and promoting melanosome synthesis. Along with melanogenesis activation, we found that MTyr–OANP treatment inhibited the growth of B16F10 cells (Fig. 3f) and arrested cells in the G2/M phase of the cell cycle (Supplementary Fig. 10), which may be induced by the upregulation of P21 and downregulation of Cyclin D1 (Fig. 3g). Furthermore, we also investigated the melanogenesis activation abilities of MTyr–OANPs on four human-derived melanoma cells (A375 cells, A2058 cells, Skmel28 cells and Mewo cells). As shown in Fig. 3h and Supplementary Fig. 11, MTyr–OANPs have been found to inhibit the growth of these melanoma cells, all with increased total melanin and tyrosinase activity. We found that MTyr–OANPs inhibited melanoma cell migration and downregulated the expression of matrix metallopeptidases 2 (MMP2) and 9 (MMP9) (Fig. 3i,j and Extended Data Fig. 1), indicating that continuous L-Tyr stimulation-induced melanin synthesis may not trigger metastasis like other melanogenesis-promoting stimuli, such as ultraviolet radiation.

Intermediates during melanogenesis suppressed glycolysis

We performed both RNA sequencing and differentially expressed genes (DEGs) analysis, coupled with pathway enrichment in control versus MTyr–OANP-treated cells to investigate the mechanism underlying the inhibitory effects of MTyr–OANPs on cell proliferation. Interestingly, the results showed that in addition to cell proliferation-related pathways, metabolic pathways in MTyr–OANP-treated cells (such as carbon metabolism, pyruvate metabolism and glycolysis/gluconeogenesis) were also significantly downregulated (Fig. 4a,b). Consistently, metabolite analysis by liquid chromatography-mass spectrometry (LC-MS) also demonstrated that there was a significant change in the metabolites of MTyr–OANP-treated cells compared with that in untreated cells (Extended Data Fig. 2a). The levels of intermediates of glycolysis, such as pyruvate, glucose 6-phosphate and fructose 1,6-bisphosphate, were found to be decreased (Fig. 4c). Since glycolysis is essential for the energy supply of tumour cells during rapid proliferation[39,40], we speculate that the process of melanogenesis reactivation may suppress B16F10 cell proliferation by inhibiting glycolysis. To prove this hypothesis, we cultured melanoma cells in 1.0 mg ml^{-1} MTyr–OANPs, with or without a reported tyrosinase activity inhibitor, α-arbutin (200 nM)[41,42], to inhibit melanogenesis. As shown in Extended Data Fig. 2b, MTyr–OANP-induced melanogenesis activation was markedly inhibited by α-arbutin supplementation. As expected, the change of metabolites in glycolysis and suppressed growth of B16F10 cells were also rescued by α-arbutin (Fig. 4d,e and Extended Data Fig. 2c). These data suggest that melanogenesis activation has a significant impact on cell metabolism, especially glycolysis.

We revealed that a rate-limiting enzyme in glycolysis, pyruvate kinase (PKM), was also shown in the other two significantly suppressed metabolism pathways (Fig. 4f). The activity of PKM in melanoma cells after MTyr–OANPs treatment decreased (Fig. 4g). The PKM inhibitor enhanced the inhibiting ability of MTyr–OANPs, while the PKM activator improved the PKM activity of cells treated with MTyr–OANPs (Fig. 4g). Seahorse analysis also indicated a decreased extracellular acidification rate (ECAR), an indicator of glycolysis, in MTyr–OANP-treated cells, and PKM activator co-treatment prevented the decrease in ECAR (Fig. 4h). These results indicate that MTyr–OANP treatment could inhibit PKM activity, thus causing glycolysis inhibition.

To determine how melanogenesis activated by MTyr–OANPs inhibits PKM activity, we first treated melanoma cells with melanin
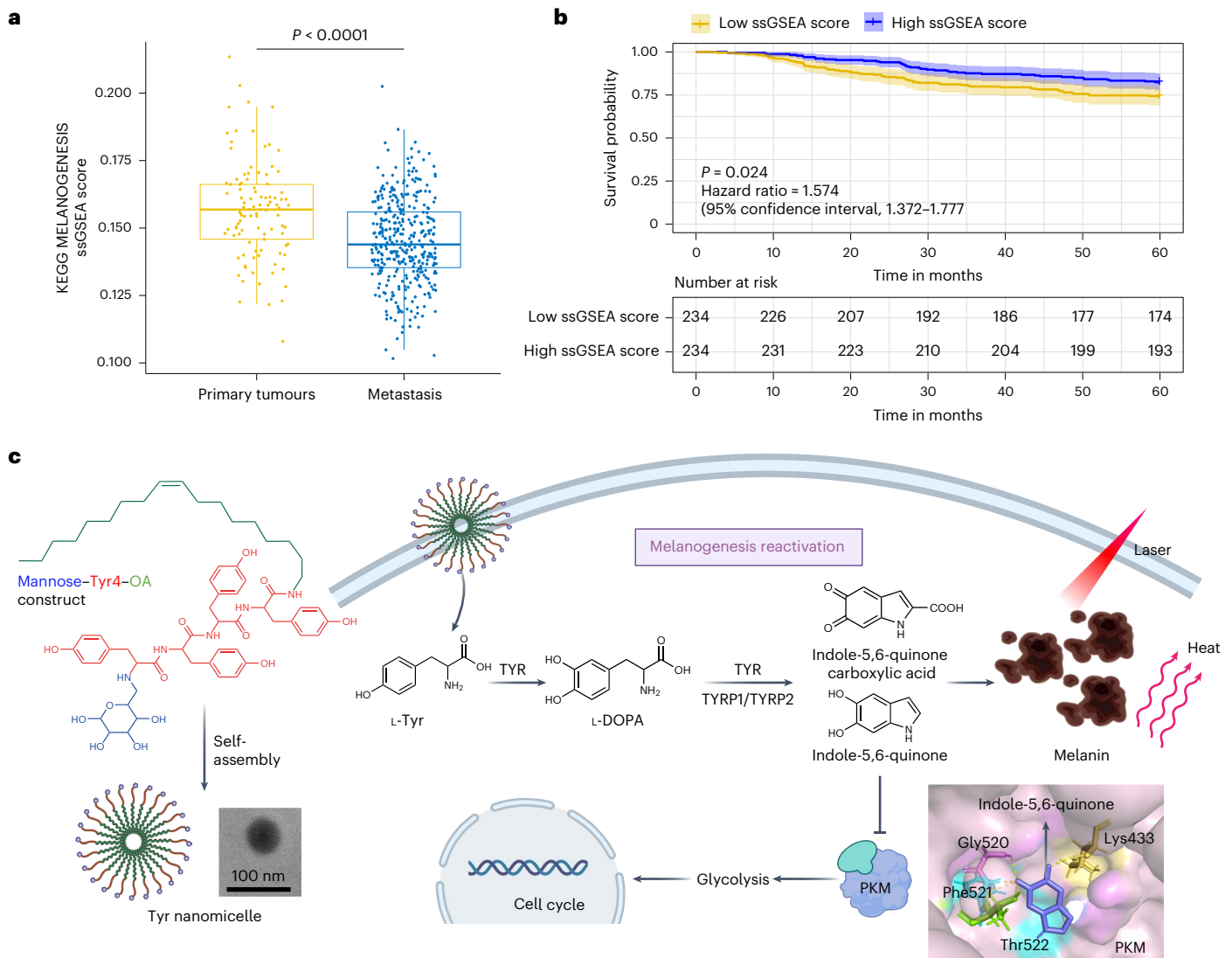
Fig. 1 | Nutrient-based metabolism reactivation strategy for melanoma treatment. a, The ssGSEA score in patients with primary and metastatic SKCM from the TCGA cohort. Primary tumours, $n = 101$ (yellow); metastasis, $n = 366$ (blue). A two-sided Wilcoxon test was used ($P < 0.0001$). Data are presented as box plots where the centre line is median, the upper bound is the 75th percentile, the lower bound is the 25th percentile, and the whiskers indicate the minimum and maximum values. Each dot represents one donor. **b**, Kaplan–Meier survival curves for 5-year survival outcomes of $n = 468$ SKCMs (101 primary solid tumours, 366 metastatic tumours and 1 additional metastatic tumour) in the TCGA cohort. 'Low ssGSEA score' (yellow line) and 'high ssGSEA score' (blue line) were estimated according to the average ssGSEA score of the 'KEGG MELANOGENESIS' gene signature. The shading is the 95% confidence interval band. Univariate Cox regression was used. The difference between the two curves was determined by the two-sided log-rank test ($P = 0.024$). **c**, MTyr–OANPs were constructed to improve the Tyr level in melanoma cells. Tyr reactivated the melanin synthesis pathway and the melanin intermediate indole-5,6-quinone inhibited PKM, thus suppressing glycolysis, which induced cell cycle arrest in melanoma cells. PTT was applied for tumour reduction by exploiting the excellent photothermal conversion performance of endogenously produced melanin. Created with BioRender.com.

and revealed that melanin itself does not affect PKM (Extended Data Fig. 2d); therefore, the intermediates during melanogenesis may play an important role. Moreover, the LC-MS results showed an increase in melanin intermediates, including L-DOPA, 5,6-dihydroxyindole (5,6-DHI) and 5,6-dihydroxyindole-2-carboxylic acid (5,6-DHICA), after MTyr–OANP treatment (Extended Data Fig. 3), and the molecular docking simulation results showed that indole-5,6-quinone docks with PKM with a binding energy of -9.19 kcal mol^{-1} (Fig. 4i), indicating specific binding[43]. Lastly, the cell growth inhibition ability of indole-5,6-quinone was decreased by the PKM inhibitor and increased by the PKM activator (Fig. 4j). These data suggested that melanogenesis reactivation produces toxic intermediates, such as indolic and quinonic compounds, which have a strong inhibiting effect on cell glycolysis owing to the affinity of quinones to PKM, thus inhibiting cell glycolysis and consequently causing cell death.

Antitumour efficacy of MTyr–OANPs in melanoma-bearing mice

The in vivo antitumour activity of MTyr–OANPs was first assessed in B16F10 melanoma-bearing mice. Before treatment, we assessed the metabolic behaviour and distribution of MTyr–OANPs in mice using positron emission tomography-computed tomography imaging by labelling MTyr–OANPs with ^{125}I. As shown in Supplementary Fig. 12, the labelling efficiency of ^{125}I-MTyr–OANPs exceeded 98%. Following the injection of ^{125}I-MTyr–OANPs into the tail vein, in the initial 10 min, a notable signal was observed throughout the entire body with the highest concentration observed in the liver (Supplementary Video 1). After 1 h, MTyr–OANPs started to be excreted through the bladder, and at post 24 h, the strong signal in the liver indicated the prolonged presence of ^{125}I-MTyr–OANPs within the body (Supplementary Fig. 13). In addition, the blood half-life of ^{125}I-MTyr–OANPs was calculated
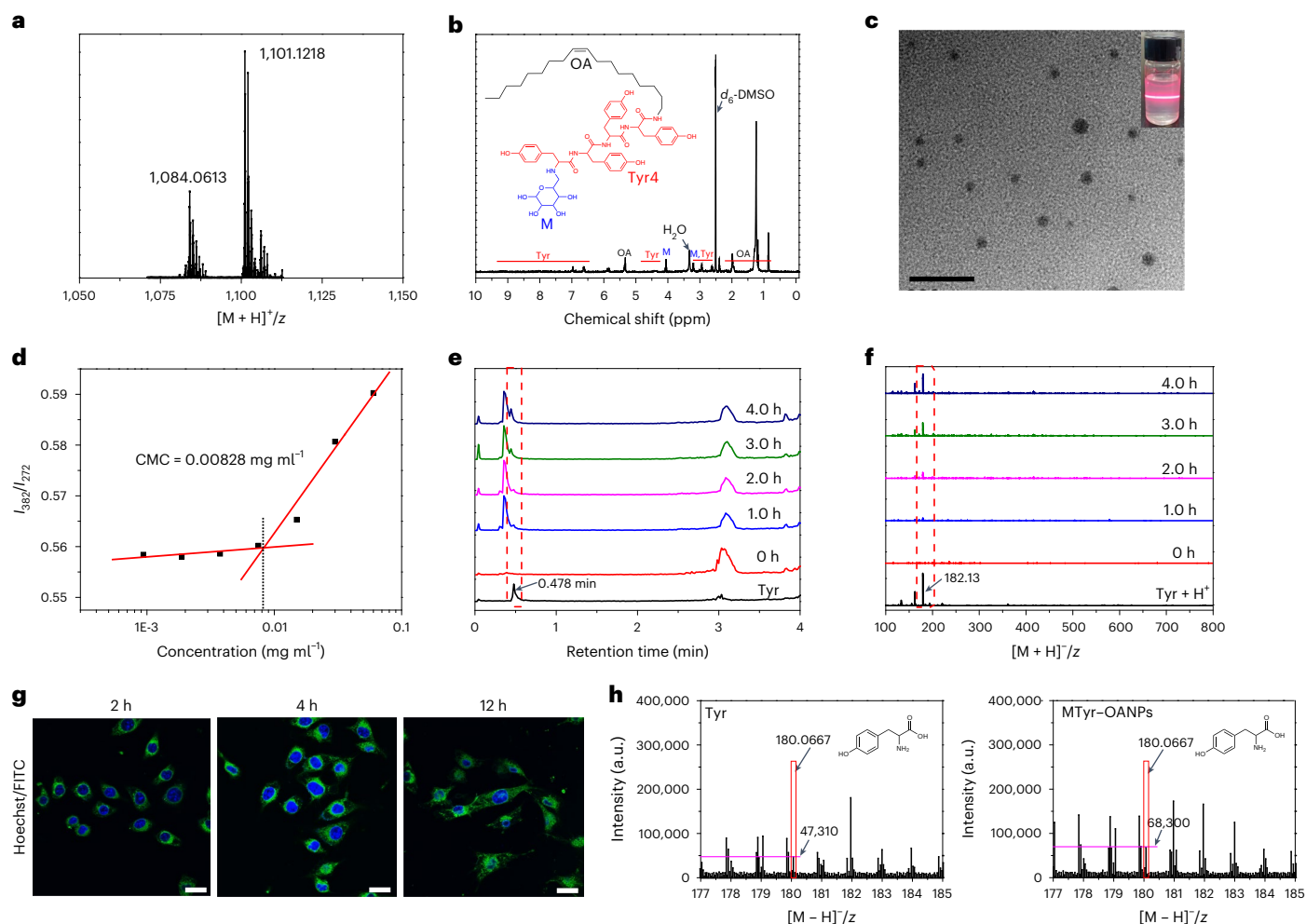
Fig. 2 | Stability, biocompatibility and delivery efficiency of MTyr−OANPs. **a**, Mass spectrum of MTyr4−OA. **b**, ¹H NMR spectrum of MTyr4−OA. **c**, TEM of MTyr−OANPs. Inset is the digital photograph of MTyr-OANPs with Tyndall effect. Scale bar, 200 μm. The experiment was repeated three times. **d**, CMC of MTyr4−OA. **e**,**f**, LC chromatograms (**e**) and mass spectrum (**f**) of the released product from MTyr−OANPs with time under peptide enzymes. **g**, Confocal microscopy images of endocytosis after incubating with MTyr−OANPs (0.5 mg ml⁻¹) for different times. MTyr−OANPs were labelled with fluorescein isothiocyanate (FITC) (green). Scale bars, 50 μm. The experiment was repeated three times. **h**, The mass spectra of intracellular ʟ-Tyr content by LC-MS.

to be approximately 22 min based on the one-phase decay (Supplementary Fig. 14).

MTyr−OANPs were found to be accumulated at the tumour site, compared with Tyr−OANPs (with no mannose moieties) (Fig. 5a), after intravenous injection, owing to the highly expressed glucose receptors of melanoma cells[44]. To further accurately determine the tumour accumulation rate, we conducted an evaluation of the distribution of ¹²⁵I-MTyr−OANPs in tumour-bearing mice. As depicted in Supplementary Figs. 15 and 16, 5 h after injection, the signal appeared in the tumour. On the basis of the initial radiation intensity (0.5 μCi), injection sample volume (100 μl), radiation intensity in tumour area (0.0086 μCi) and the isolated tumour volume (0.256 cm³), the accumulation rate of ¹²⁵I-MTyr−OANPs, yielding a value of $k_{accumulation}$ 4.4%, we determined that the minimum required concentration for $V_{injection}$ should be around 6.8 mg ml⁻¹.

Under this dosage, we found that tumour growth in melanoma-bearing mice was markedly inhibited by MTyr−OANPs and survival in tumour-bearing mice was also improved (Fig. 5b−e). The immunohistochemistry results illustrated the low Ki67 expression in MTyr−OANP-treated mouse tumours (Fig. 5f,g). We determined an increase in tyrosinase activity and total melanin content within the mouse tumours treated with MTyr−OANPs (Fig. 5h,i). In addition, as illustrated in Extended Data Fig. 4a,b, the tumours exhibited a darker colour,

and Fontana-Masson staining of tumour tissue sections also showed increased melanin following MTyr−OANP treatment. Moreover, the expression of the glycolysis-related genes *Hk1*, *Pfkm* and *Pkm2* also decreased (Fig. 5j and Extended Data Fig. 4c−g), which indicated the inhibition of glucose metabolism in vivo.

MTyr−OANP-induced phenotypic change for PTT
Since a high intracellular melanin content was found in MTyr−OANP-treated B16F10 cells (see the cell pellets isolated in Fig. 6a), and melanin is an excellent natural photothermal reagent in the near-infrared (NIR) region, pigmented melanoma cells become sensitive to NIR-laser treatment. As shown in Fig. 6b,c, under 808 nm laser irradiation (0.28 W cm⁻²), the temperature of MTyr−OANP-treated cells increased to 44.0 ± 0.4 °C in 5 min. By contrast, the temperature of untreated cells increased only ~1.5 °C. Moreover, we also observed that MTyr−OANP-treated cells showed a significant decrease in the expression of heat shock proteins 70 (HSP70) and 90 (HSP90) compared with that of MTyr−OANP-untreated B16F10 cells with or without heat treatment (Fig. 6d). These results indicated that MTyr−OANP-treated cells were more vulnerable to heat stress. Thus, MTyr−OANP-treated cells would enable enhanced PTT under NIR-laser treatment. By irradiating MTyr−OANP-treated cells with an 808 nm laser, we found that it significantly inhibited the viability of B16F10 cells compared with
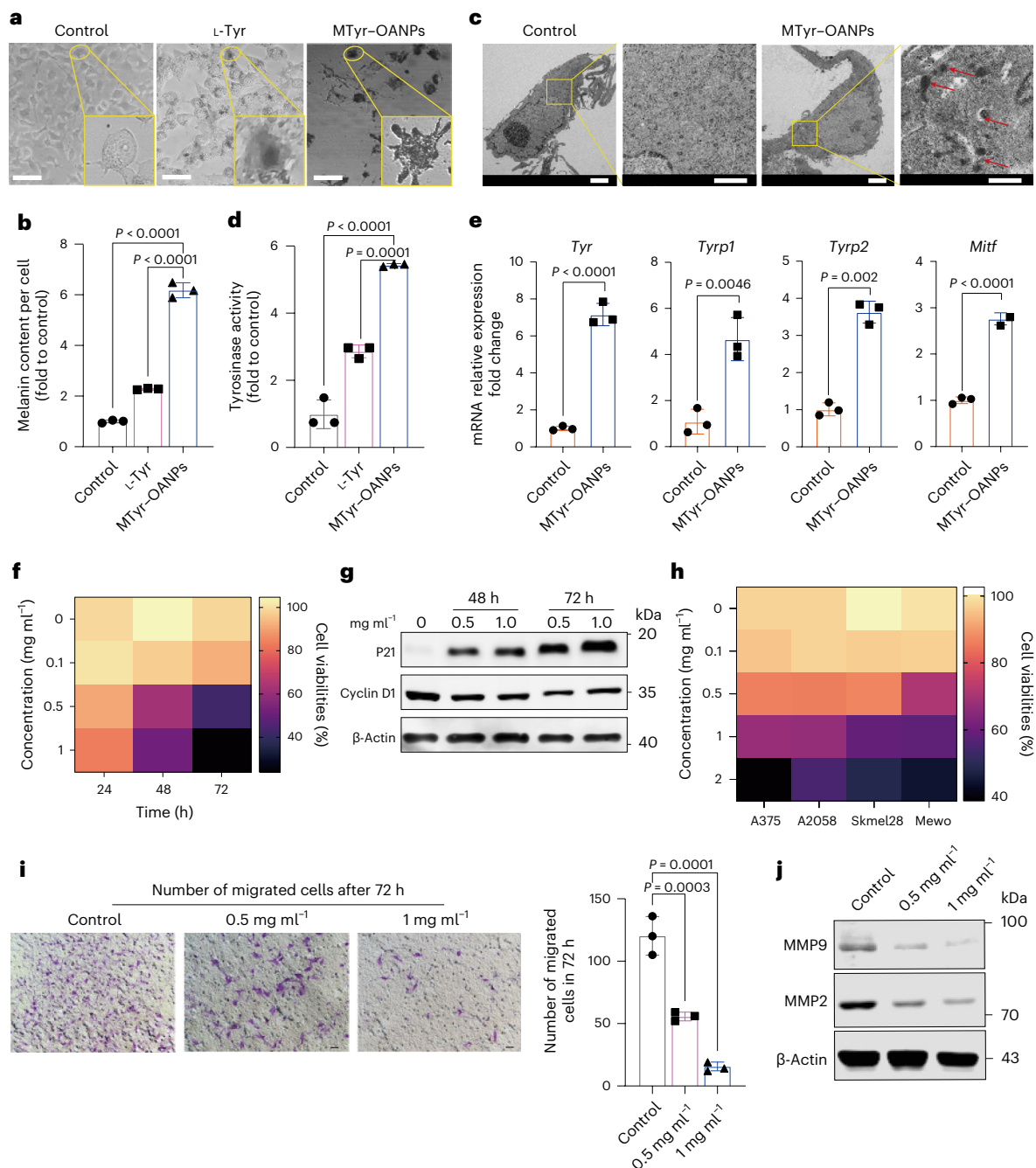
Fig. 3 | Quantitative analysis of efficiency of MTyr–OANPs in promoting melanogenesis and inhibiting growth and migration of melanoma cells.
a, Microscopy images showing the cell morphology of control, L-Tyr-treated and MTyr–OANP-treated cells. Scale bars, 50 μm. The experiment was repeated three times. **b**, Intracellular melanin content (*n* = 3 biological replicates). **c**, TEM images of melanosomes in B16F10 cells before and after MTyr–OANP treatment. Scale bars, 200 μm in the low-magnification images and 500 μm for the enlarged images. Red arrows represent melanosomes. The experiment was repeated three times. **d**, Tyrosinase activities of B16F10 cells co-cultured with MTyr–OANPs for 48 h. **e**, Analysis of *Tyr*, *Tyrp1*, *Tyrp2* and *Mitf* expression using qPCR (*n* = 3 biological replicates). **f**, Cell viabilities of B16F10 cells incubated with

0 mg ml⁻¹, 0.1 mg ml⁻¹, 0.5 mg ml⁻¹ and 1 mg ml⁻¹ MTyr–OANPs for 24 h, 48 h and 72 h, respectively (*n* = 6 biological replicates). **g**, Western blot of the cell cycle-related proteins P21 and Cyclin D1. The experiment was repeated three times. **h**, Cell viabilities of A375 cells, A2058 cells, Skmel28 cells and Mewo cells incubated with 0 mg ml⁻¹, 0.1 mg ml⁻¹, 0.5 mg ml⁻¹, 1 mg ml⁻¹ and 2 mg ml⁻¹ MTyr–OANPs for 72 h (*n* = 6 biological replicates). **i**, Transwell assay for control and MTyr–OANP-treated cells. Scale bars, 40 μm (*n* = 3 biological replicates). **j**, Western blot of the expression of MMP9 and MMP2. The experiment was repeated three times. Data are presented as mean ± s.d. *P* values were determined using Student's *t*-test (unpaired, two-tailed) or one-way ANOVA followed by post hoc Tukey's test.

that of cells treated with MTyr–OANPs alone or the laser alone (Fig. 6e and Extended Data Fig. 5a).

Notably, owing to the increased melanin content in mouse tumours (Extended Data Fig. 4a,b) after MTyr–OANP treatment, under 808 nm laser irradiation for 5 min (0.28 W cm⁻²), the temperature of tumours in

the MTyr–OANP group increased to 44.3 ± 0.1 °C (Fig. 6f and Extended Data Fig. 5b). Immunohistochemistry assays showed that the expression levels of the heat damage resistance proteins HSP70 and HSP90 were also significantly reduced in mouse tumours (Fig. 6g). As shown in Fig. 6h and Extended Data Fig. 5c, the volume of mouse tumours was
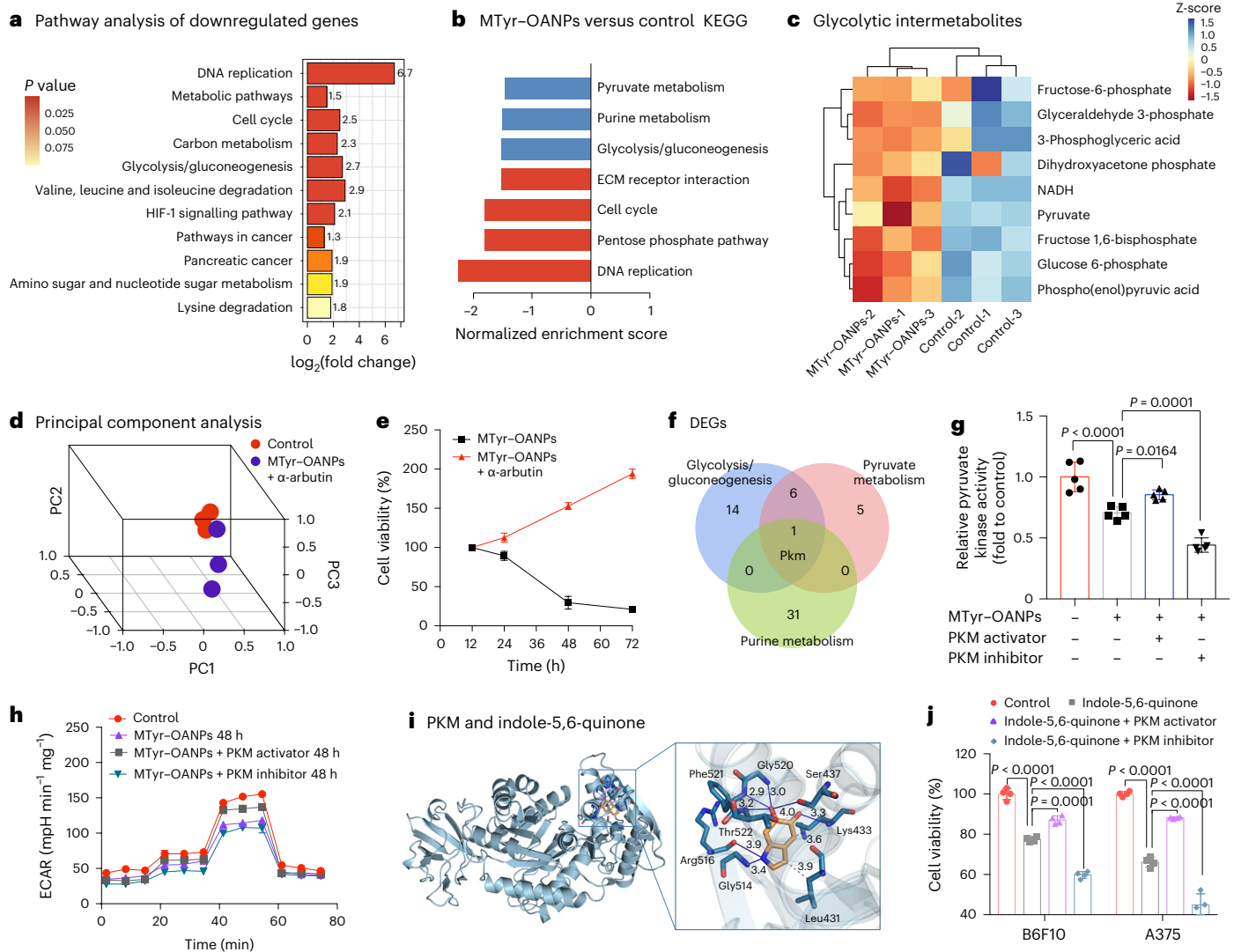
Fig. 4 | MTyr–OANP-induced tyrosinase activation and glycolysis suppression. a, Pathway enrichment analysis of DEGs downregulated in MTyr–OANP-treated versus untreated cells with fold change ≥ 1.5, $P < 0.075$ and false discovery rate < 0.05 ($n = 3$ biological replicates). **b**, Bar plots showing the downregulated pathways in the comparison of MTyr–OANPs versus control group (DEGs with $\log_2$(fold change) ≥ 1 and adjusted P value < 0.05 were then identified; $n = 3$ biological replicates); ECM represents extracellular matrix. **c**, Heat map of glycolysis intermediate metabolites ($P < 0.05$, $n = 3$ biological replicates). NADH represents nicotinamide adenine dinucleotide. The colour bar shows Z-score. **d**, PCA of metabolites in MTyr–OANP- and α-arbutin-co-treated versus control cells ($n = 3$ biological replicates). **e**, Cell viabilities of MTyr–OANP-treated, MTyr–OANP-co-treated and α-arbutin-co-treated cells with time ($n = 5$ biological replicates). **f**, Venn map of glycolysis/gluconeogenesis, pyruvate metabolism and purine metabolism DEGs. **g**, Pyruvate kinase activities of B16F10 cells after incubation with MTyr–OANPs, MTyr–OANPs + PKM inhibitor PKM2-IN-1 and MTyr–OANPs + PKM activator TEPP-46 ($n = 5$ biological replicates). **h**, ECAR of cells with the same treatment as in **g** ($n = 3$ biological replicates). **i**, Molecular docking analysis of indole-5,6-quinone and PKM (left) and the enlarged image of interaction; shading represents the cartoon image of the docking pocket (right). The solid blue line indicates hydrogen bonding and the grey dashed line indicates hydrophobic forces. **j**, Cell viabilities of indole-5,6-quinone, indole-5,6-quinone + PKM inhibitor PKM2-IN-1 and indole-5,6-quinone + PKM activator TEPP-46-treated, co-treated cells after 72 h ($n = 4$ biological replicates). Data are represented as mean ± s.d., and P values were determined using Student's t-test (unpaired, two-tailed) or one-way ANOVA followed by post hoc Tukey's test.

significantly reduced under MTyr–OANPs and laser co-treatment. In addition, the tumours in the 'MTyr–OANPs + laser' group completely disappeared after only 6 days of treatment (Fig. 6h and Extended Data Fig. 5c). More excitingly, during the following 49 days of observation, the tumours in the 'MTyr–OANPs + laser' group did not recur (Extended Data Fig. 5d). Notably, those treated with MTyr–OANPs plus 808 nm laser had a significantly increased life expectancy when compared with that of PBS-treated mice (Fig. 6i). In addition, the histological analysis (haematoxylin and eosin (H&E)) in Extended Data Fig. 5e shows that the 'MTyr–OANPs + laser' cotreatment exhibited the most necrotic and apoptotic cells inside the mouse tumours.

Since the photothermal effect in the 'MTyr–OANPs + laser' group is a result of the increased melanin production, we further verify the efficacy of PTT alone by adding a control group with an equivalent thermal effect to the 'MTyr–OANPs + laser' group by increasing the laser power intensity. Through screening different laser power intensities, we found that a similar heating effect to that observed in the 'MTyr–OANPs + laser' group could be achieved when the power density was increased to 0.32 W cm^{-2} (Extended Data Fig. 6a–c). Subsequently, under this power density, we demonstrated that photothermal effect alone, after increasing melanin production, inhibited melanoma growth by ~55.2% (Extended Data Fig. 6d,e).

Conclusion

Our nutrient-based metabolism reactivation strategy has been demonstrated to be effective for melanoma tumour treatment. L-Tyr
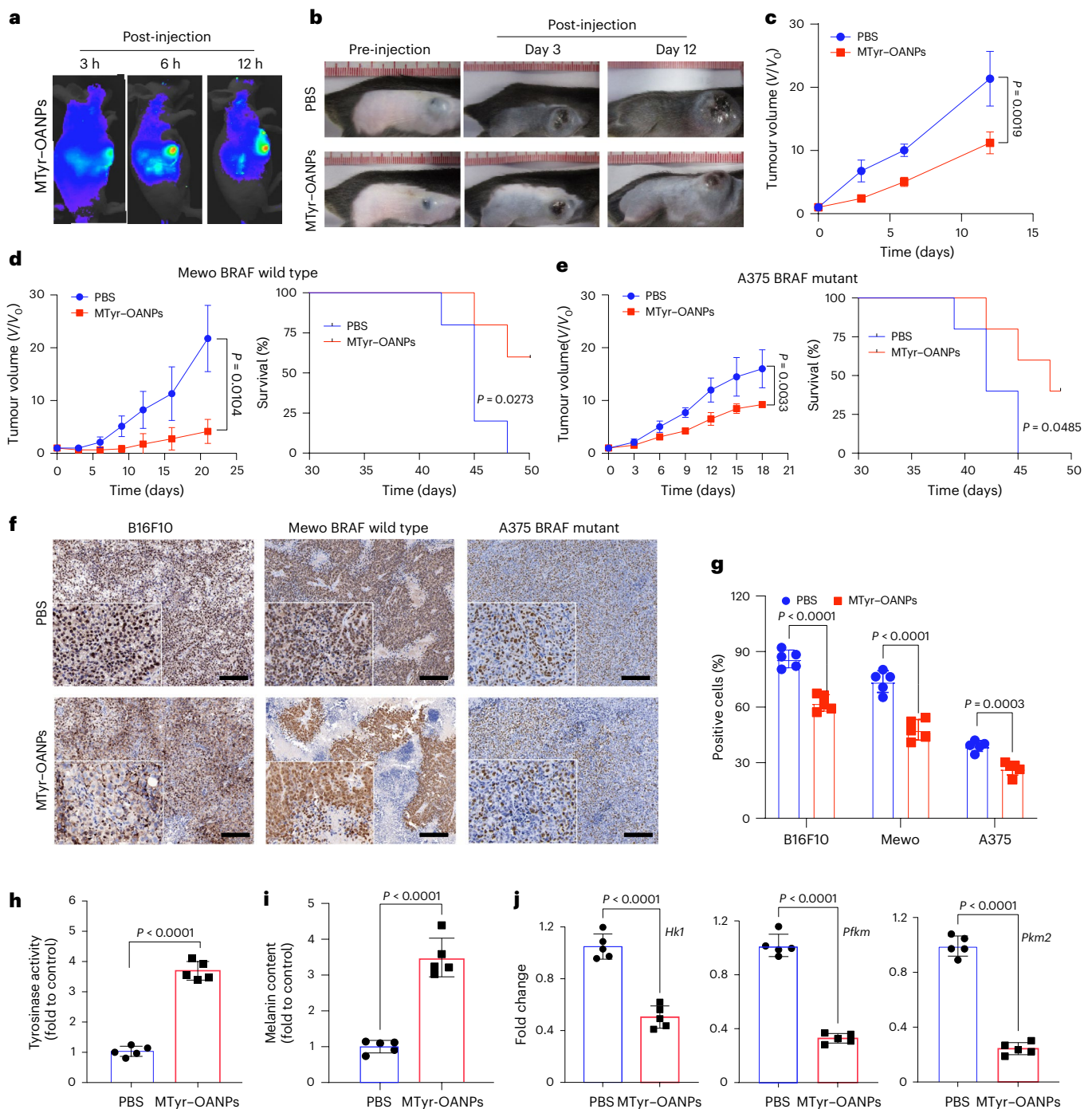
Fig. 5 | In vivo antitumour activity of MTyr–OANPs in melanoma-bearing mice. a, Fluorescence images of the in vivo distribution of Tyr–OANPs and MTyr–OANPs after intravenous injection; Cyanine 5.5 was used to label Tyr–OANPs and MTyr–OANPs. **b**, Representative images of B16F10 tumour-bearing mice in the PBS and MTyr–OANP groups during 12 days of treatment ($n = 5$ biological replicates). **c**, Tumour growth curves for B16F10 tumours (V/V_0) throughout the 12 days treated with PBS and MTyr–OANPs ($n = 5$ biological replicates). **d,e**, Tumour growth curves of Mewo (**d**) and A375 (**e**) tumours (V/V_0) throughout the 15 days treated with PBS and MTyr–OANPs and Kaplan–Meier survival curve of tumour-bearing mice in each group ($n = 5$ biological replicates).

f, Immunohistochemistry results of Ki67 in mouse tumours. The experiment was repeated three times. Scale bars, 200 μm. **g**, Quantitative analysis results of images in **f** ($n = 5$ images from different fields of view). **h,i**, Tyrosinase activity (**h**) and melanin content (**i**) of mouse tumours in **b** ($n = 5$ biological replicates). **j**, mRNA expression of *Hk1*, *Pfkm* and *Pkm2* in melanoma cells treated with MTyr–OANPs in vivo ($n = 5$ biological replicates). Data are represented as mean ± s.d., and P values were determined using Student's t-test (unpaired, two-tailed). The difference between the two survival curves was determined by the two-sided log-rank test.

supplementation via MTyr–OANPs prominently reactivated the suppressed melanogenesis-related metabolism in melanoma cells, and the increased intermediates during melanogenesis could suppress cell glycolysis, thus retarding melanoma growth, which is a different mechanism for pro-melanogenesis-induced tumour inhibition[45]. This proposed concept is applicable to both eumelanic phenotype and pheomelanic phenotype melanomas because during the synthesis of both eumelanins and pheomelanins, L-Tyr serves as the substrate. L-Tyr
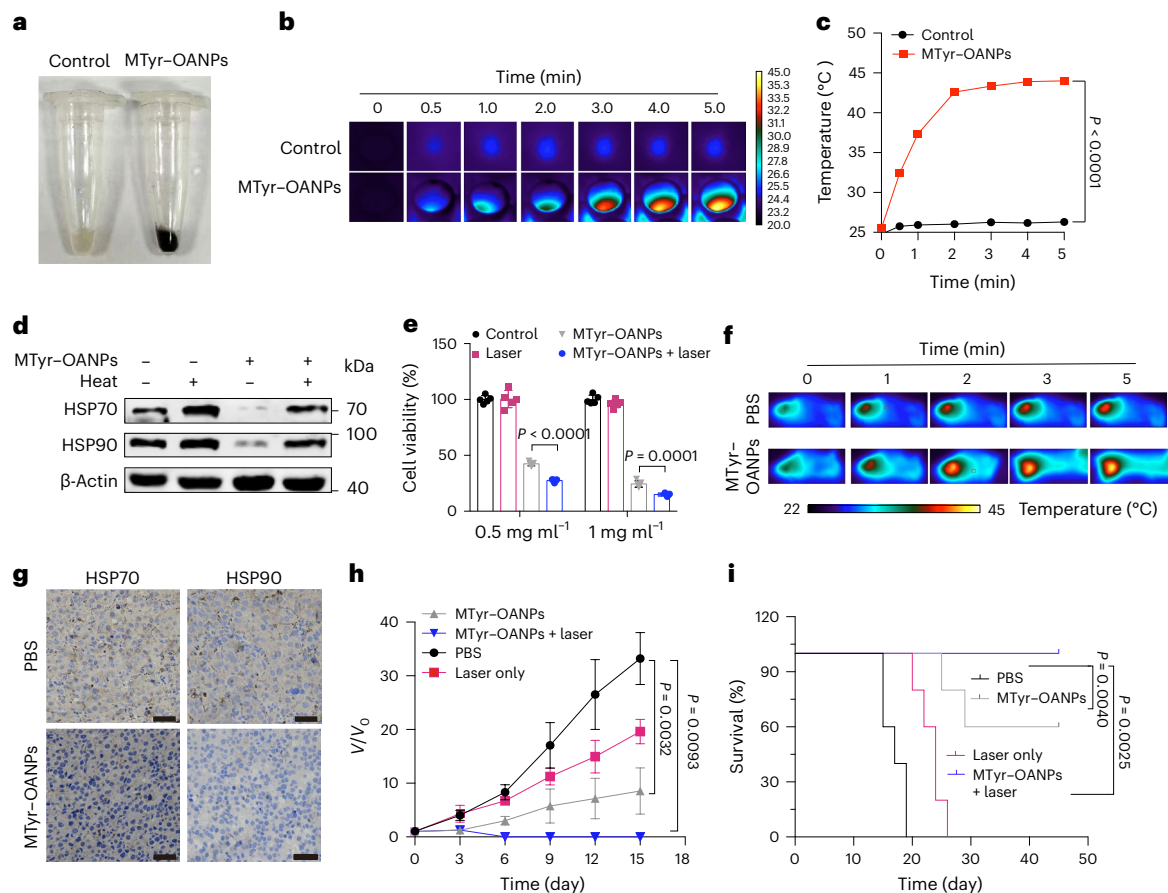
Fig. 6 | Pigmented cell phenotypes enhanced cell death in response to 808 nm laser irradiation. a, Cell pellets isolated before and after treatment with 1 mg ml^{-1} MTyr–OANPs for 72 h. The experiment was repeated three times. **b**, Representative infrared thermal images of 808 nm laser-induced photothermal conversion of B16F10 cells seeded on a 96-well plate. **c**, Temperature increase curves versus irradiation time based on the infrared thermal images in **b** ($n = 3$ biological replicates). **d**, The HSP90 and HSP70 level measured by western blotting after heat treatment. The experiment was repeated three times. **e**, Cell viabilities of B16F10 cells incubated with 0.5 mg ml^{-1} and 1 mg ml^{-1} MTyr–OANPs for 72 h and/or treated with an 808 nm laser for 5 min ($n = 5$ biological replicates). **f**, Representative infrared thermal images under 808 nm laser irradiation of tumours with or without MTyr–OANPs treatment. The experiment was repeated three times. **g**, Representative immunohistochemistry images of HSP70 and HSP90 of mouse tumours. The experiments were repeated three times. Scale bars, 50 μm. **h**, Growth curves for B16F10 tumours (V/V_0) throughout the 15 days treated with PBS, MTyr–OANPs, 808 nm laser and MTyr–OANPs + 808 nm laser ($n = 5$ biological replicates). **i**, Kaplan–Meier survival curve of B16F10 tumour-bearing mice in each group ($n = 5$ biological replicates). Data are represented as mean ± s.d., and P values were determined using Student's t-test (unpaired, two-tailed) or one-way ANOVA followed by post hoc Tukey's test. The difference in the survival curves was determined by the two-sided log-rank test.

can induce translocation of tyrosinase from the *trans*-Golgi network to melanosomes and stimulation of tyrosinase maturation, thus resulting in an increase in melanin production. Our strategy may encounter limitations in certain melanomas where activation or induction of tyrosinase is not feasible. For instance, in amelanotic melanoma cells, tyrosinase stability may be compromised, leading to degradation within the endoplasmic reticulum before reaching the melanosome for L-Tyr oxidation[46]. In addition, microphthalmia-associated transcription factor (MITF) activity is required for tyrosinase production and it has been shown that ubiquitination and degradation of MITF are regulated by neuroblastoma RAS viral(v-ras) oncogene homolog (NRAS) or v-Raf murine sarcoma viral oncegene homolog B (BRAF) mutations in melanomas[47–49]. The responses of these tumours to L-Tyr addition in conjunction with MITF expression levels will be further investigated in the future. We found that continuous L-Tyr stimulation to induce melanin synthesis suppressed the migration of melanoma cells but further experiments were needed to evaluate the anti-metastatic potential of L-Tyr nanomicelles. Besides melanoma, our strategy also has potential application in other tumours. For example, gluconeogenesis is a typical metabolic pathway of liver cells that produces glucose or glycogen, which was downregulated in liver tumour cells[16,17]. In addition, the

CYP1A1 pathway of oestrogen metabolism in ovarian cancer cells is inhibited and it is related to cell apoptosis[30]. Therefore, reactivating these downregulated metabolic pathways may also inhibit tumour growth.

It is well known that nutrients are involved in maintaining the metabolism of organisms. Here we found that the supplemented L-Tyr was directly utilized for melanin synthesis, not for cell proliferation. In accordance with this, some nutrients, including glutamine[50], mannose[51] and α-linolenic acids[30], have also been reported to inhibit the growth of a specific tumour via a particular metabolic pathway. For example, mannose can inhibit the growth of tumours with low expression of phosphomannose isomerase[51], and glutamine can slow the growth of melanoma in a hypoxic tumour microenvironment[50]. These studies, together with our results, indicated that under certain conditions, a particular nutrient may inhibit tumour growth. Since nutrients are safe and easily acquired in daily diet, they are promising for clinical practice. The key lays in promoting their poor targeting efficiency owing to the limited intake of free nutrients by tumour cells, so supplementation with free nutrients may not be efficient for tumour suppression. As nanotechnology opens a promising window for drug delivery and tumour treatment, nanoparticles, including liposomes[52]

and metal–organic frameworks[53], can also become the highly effective approaches for nutrient supplementation in tumour treatment.

Reactivating downregulated metabolic pathways using nutrients for tumour treatment has also led to cascade therapeutic opportunities. Recently, clinical data have shown that combination therapies can achieve better results than monotherapy in tumour treatment, and the 'one–two punch' model for the precision treatment of tumours has achieved greater outcomes[54]. Inducing weakness in tumour cells first, followed by exploiting their vulnerability for cascade treatment, will highly improve the treatment efficacy[55]. In another study, supplementation with arginine in brain metastases increased the content of nitric oxide, which can enhance the effect of radiation therapy[56]. Nutrients used for tumour treatment might be transformed into metabolites, and these functional metabolites could be exploited by other therapies.

Our results provide conclusive evidence that, like inhibiting hyperactivated metabolic pathways, reactivating hypoactive metabolic pathways has the potential to counteract tumour growth. As a new direction along the reverse thinking logic, this study suggests that this nutrient-based metabolism reactivation strategy will inspire broad applications in the treatment of other diseases associated with metabolic disorders.

Online content

Any methods, additional references, Nature Portfolio reporting summaries, source data, extended data, supplementary information, acknowledgements, peer review information; details of author contributions and competing interests; and statements of data and code availability are available at https://doi.org/10.1038/s41565-024-01690-6.

References

1. Faubert, B., Solmonson, A. & DeBerardinis, R. J. Metabolic reprogramming and cancer progression. *Science* **368**, 152–163 (2020).
2. Martinez-Reyes, I. & Chandel, N. S. Cancer metabolism: looking forward. *Nat. Rev. Cancer* **21**, 669–680 (2021).
3. Heiden, M. G. V., Cantley, L. C. & Thompson, C. B. Understanding the Warburg effect: the metabolic requirements of cell proliferation. *Science* **324**, 1029–1033 (2009).
4. Schiliro, C. & Firestein, B. L. Mechanisms of metabolic reprogramming in cancer cells supporting enhanced growth and proliferation. *Cells* **10**, 1056–1097 (2021).
5. Koundouros, N. & Poulogiannis, G. Reprogramming of fatty acid metabolism in cancer. *Br. J. Cancer* **122**, 4–22 (2020).
6. Eniafe, J. & Jiang, S. The functional roles of TCA cycle metabolites in cancer. *Oncogene* **40**, 3351–3363 (2021).
7. Nakhle, J., Rodriguez, A. M. & Vignais, M. L. Multifaceted roles of mitochondrial components and metabolites in metabolic diseases and cancer. *Int. J. Mol. Sci.* **21**, 4405–4436 (2020).
8. Abdel-Wahab, A. F., Mahmoud, W. & Al-Harizy, R. M. Targeting glucose metabolism to suppress cancer progression: prospective of anti-glycolytic cancer therapy. *Pharmacol. Res.* **150**, 104511 (2019).
9. Di Cosimo, S. et al. Lonidamine: efficacy and safety in clinical trials for the treatment of solid tumors. *Drugs Today* **39**, 157–174 (2003).
10. Qi, H. et al. Shikonin induced apoptosis mediated by endoplasmic reticulum stress in colorectal cancer cells. *J. Cancer* **13**, 243–252 (2022).
11. Dowsett, M. et al. Aromatase inhibitors versus tamoxifen in early breast cancer: patient-level meta-analysis of the randomised trials. *Lancet* **386**, 1341–1352 (2015).
12. Ma, C. X., Reinert, T., Chmielewska, I. & Ellis, M. J. Mechanisms of aromatase inhibitor resistance. *Nat. Rev. Cancer* **15**, 261–275 (2015).
13. Ruijtenberg, S. & van den Heuvel, S. Coordinating cell proliferation and differentiation: antagonism between cell cycle regulators and cell type-specific gene expression. *Cell Cycle* **15**, 196–212 (2016).
14. Gaude, E. & Frezza, C. Tissue-specific and convergent metabolic transformation of cancer correlates with metastatic potential and patient survival. *Nat. Commun.* **7**, 13041 (2016).
15. Garrett, M. et al. Metabolic characterization of isocitrate dehydrogenase (IDH) mutant and IDH wildtype gliomaspheres uncovers cell type-specific vulnerabilities. *Cancer Metab.* **6**, 4 (2018).
16. Suzuki, H. et al. Metabolic alteration in hepatocellular carcinoma: mechanism of lipid accumulation in well-differentiated hepatocellular carcinoma. *Can. J. Gastroenterol. Hepatol.* **2021**, 8813410 (2021).
17. Ma, R. et al. Switch of glycolysis to gluconeogenesis by dexamethasone for treatment of hepatocarcinoma. *Nat. Commun.* **4**, 2508 (2013).
18. Soballe, P. W. & Herlyn, M. Cellular pathways leading to melanoma differentiation—therapeutic implications. *Melanoma Res.* **4**, 213–223 (1994).
19. Lei, M. J., Dong, Y., Sun, C. X. & Zhang, X. H. Resveratrol inhibits proliferation, promotes differentiation and melanogenesis in HT-144 melanoma cells through inhibition of MEK/ERK kinase pathway. *Microb. Pathog.* **111**, 410–413 (2017).
20. Chaabane, F., Pinon, A., Simon, A., Ghedira, K. & Chekir-Ghedira, L. Phytochemical potential of *Daphne gnidium* in inhibiting growth of melanoma cells and enhancing melanogenesis of B16-F0 melanoma. *Cell Biochem. Funct.* **31**, 460–467 (2013).
21. Sung, J. Y. & Cheong, J. H. New immunometabolic strategy based on cell type-specific metabolic reprogramming in the tumor immune microenvironment. *Cells* **11**, 768 (2022).
22. Elia, I., Schmieder, R., Christen, S. & Fendt, S. M. Organ-specific cancer metabolism and its potential for therapy. *Handb. Exp. Pharmacol.* **233**, 321–353 (2016).
23. Costello, L. C. & Franklin, R. B. Novel role of zinc in the regulation of prostate citrate metabolism and its implications in prostate cancer. *Prostate* **35**, 285–296 (1998).
24. Franklin, R. B. & Costello, L. C. Zinc as an anti-tumor agent in prostate cancer and in other cancers. *Arch. Biochem. Biophys.* **463**, 211–217 (2007).
25. Goode, D. R., Totten, R. K., Heeres, J. T. & Hergenrother, P. J. Identification of promiscuous small molecule activators in high-throughput enzyme activation screens. *J. Med. Chem.* **51**, 2346–2349 (2008).
26. Williams, K. P. & Scott, J. E. Enzyme assay design for high-throughput screening. *Methods Mol. Biol.* **565**, 107–126 (2009).
27. Werle, M. & Bernkop-Schnurch, A. Strategies to improve plasma half life time of peptide and protein drugs. *Amino Acids* **30**, 351–367 (2006).
28. Casero, R. A., Stewart, T. M. & Pegg, A. E. Polyamine metabolism and cancer: treatments, challenges and opportunities. *Nat. Rev. Cancer* **18**, 681–695 (2018).
29. Frezza, C. Histidine metabolism boosts cancer therapy. *Nature* **559**, 484–485 (2018).
30. Pal, P., Hales, K., Petrik, J. & Hales, D. B. Pro-apoptotic and anti-angiogenic actions of 2-methoxyestradiol and docosahexaenoic acid, the biologically derived active compounds from flaxseed diet, in preventing ovarian cancer. *J. Ovarian Res.* **12**, 49–65 (2019).
31. Tapsell, L. C., Neale, E. P., Satija, A. & Hu, F. B. Foods, nutrients, and dietary patterns: interconnections and implications for dietary guidelines. *Adv. Nutr.* **7**, 445–454 (2016).

32. Fanzo, J. et al. Nutrients, foods, diets, people: promoting healthy eating. *Curr. Dev. Nutr.* **4**, nzaa069 (2020).

33. Zhuang, C. et al. Small molecule-drug conjugates: a novel strategy for cancer-targeted treatment. *Eur. J. Med. Chem.* **163**, 883–895 (2019).

34. Donaldson, M. S. Nutrition and cancer: a review of the evidence for an anti-cancer diet. *Nutr. J.* **3**, 19 (2004).

35. De Cicco, P. et al. Nutrition and breast cancer: a literature review on prevention, treatment and recurrence. *Nutrients* **11**, 1514 (2019).

36. Kim, M. et al. Thermohydrogel containing melanin for photothermal cancer therapy. *Macromol. Biosci.* **17**, 1600371 (2017).

37. Zhao, X. et al. Melanin-inspired design: preparing sustainable photothermal materials from lignin for energy generation. *ACS Appl. Mater. Interfaces* **13**, 7600–7607 (2021).

38. Wang, K. et al. Melanin-perovskite composites for photothermal conversion. *Adv. Energy Mater.* **9**, 1901753 (2019).

39. Lunt, S. Y. & Vander Heiden, M. G. Aerobic glycolysis: meeting the metabolic requirements of cell proliferation. *Annu. Rev. Cell Dev. Biol.* **27**, 441–464 (2011).

40. Gatenby, R. A. & Gillies, R. J. Why do cancers have high aerobic glycolysis? *Nat. Rev. Cancer* **4**, 891–899 (2004).

41. Saeedi, M., Khezri, K., Zakaryaei, A. S. & Mohammadamini, H. A comprehensive review of the therapeutic potential of alpha-arbutin. *Phytother. Res.* **35**, 4136–4154 (2021).

42. Zolghadri, S. et al. A comprehensive review on tyrosinase inhibitors. *J. Enzym. Inhib. Med. Chem.* **34**, 279–309 (2019).

43. Liu, J. L. et al. Spectroscopy and molecular docking analysis reveal structural specificity of flavonoids in the inhibition of alpha-glucosidase activity. *Int. J. Biol. Macromol.* **152**, 981–989 (2020).

44. Prakash, J. et al. Tumor-targeted intracellular delivery of anticancer drugs through the mannose-6-phosphate/insulin-like growth factor II receptor. *Int. J. Cancer* **126**, 1966–1981 (2010).

45. Sarna, M., Krzykawska-Serda, M., Jakubowska, M., Zadlo, A. & Urbanska, K. Melanin presence inhibits melanoma cell spread in mice in a unique mechanical fashion. *Sci. Rep.* **9**, 9280 (2019).

46. Halaban, R. et al. Aberrant retention of tyrosinase in the endoplasmic reticulum mediates accelerated degradation of the enzyme and contributes to the dedifferentiated phenotype of amelanotic melanoma cells. *Proc. Natl Acad. Sci. USA* **94**, 6210–6215 (1997).

47. Wellbrock, C. & Arozarena, I. Microphthalmia-associated transcription factor in melanoma development and MAP-kinase pathway targeted therapy. *Pigment Cell Melanoma Res.* **28**, 390–406 (2015).

48. Zhao, X., Fiske, B., Kawakami, A., Li, J. & Fisher, D. E. Regulation of MITF stability by the USP13 deubiquitinase. *Nat. Commun.* **2**, 414 (2011).

49. Wu, M. et al. c-Kit triggers dual phosphorylations, which couple activation and degradation of the essential melanocyte factor Mi. *Genes Dev.* **14**, 301–312 (2000).

50. Gabra, M. B. I. et al. Dietary glutamine supplementation suppresses epigenetically-activated oncogenic pathways to inhibit melanoma tumour growth. *Nat. Commun.* **11**, 3326 (2020).

51. Gonzalez, P. S. et al. Mannose impairs tumour growth and enhances chemotherapy. *Nature* **563**, 719 (2018).

52. Allen, T. M. & Cullis, P. R. Liposomal drug delivery systems: from concept to clinical applications. *Adv. Drug Deliv. Rev.* **65**, 36–48 (2013).

53. Wu, M. X. & Yang, Y. W. Metal–organic framework (MOF)-based drug/cargo delivery and cancer therapy. *Adv. Mater.* **29**, 1606134 (2017).

54. Zahorowska, B., Crowe, P. J. & Yang, J. L. Combined therapies for cancer: a review of EGFR-targeted monotherapy and combination treatment with other drugs. *J. Cancer Res. Clin. Oncol.* **135**, 1137–1148 (2009).

55. Wang, C. et al. Inducing and exploiting vulnerabilities for the treatment of liver cancer. *Nature* **574**, 268–272 (2019).

56. Marullo, R. et al. The metabolic adaptation evoked by arginine enhances the effect of radiation in brain metastases. *Sci. Adv.* **7**, eabg1964 (2021).

Methods

Regents

L-Tyr (PubChem ID 6057), L-DOPA (PubChem ID 6047), indole-5,
6-quinone (PubChem ID 440728), indole-5,6-quinone carboxylic acid
(PubChem ID 46173450), 5,6-DHI (PubChem ID 114683) and 5,6-DHICA
(PubChem ID 119405) were purchased from Adamas-Beta, Shanghai
Titan Scientific; Tyr-Tyr-Tyr-Tyr (Tyr4) and mannose-Tyr-Tyr-Tyr-Tyr
(MTyr4) peptide were purchased from Nanjing Yuan Peptide Biotech-
nology; ^{125}I-NaI solution was provided by Shanghai Xinke Pharmaceuti-
cal. Oleylamine, dimethyl sulfoxide (DMSO, SafeDry), tetrahydrofuran
(THF, SafeDry), 5-carboxyfluorescein, N-hydroxysuccinimide (NHS)
and 3-(3-dimethylaminopropyl)-1-ethylcarbodiimide hydro-
chloride (EDC·HCl) were all purchased from Sigma-Aldrich.
PKM2-IN-1(HY-103617) and TEPP-46(HY-18657) were purchased from
MedChemExpress. Pyruvate kinase activity assay kit (D799443-0050)
was purchased from Sangon Biotech. All other reagents were purchased
from commercial resources and used as received.

Synthesis of amphipathic MTyr4−OA

Oleylamine (120 mg, 0.45 mmol), NHS (34.5 mg, 0.30 mmol) and
EDC·HCl (57.5 mg, 0.30 mmol) were dissolved in 15 ml THF. Then
the system was kept in an ice bath under argon atmosphere. Subse-
quently, 10 ml DMSO containing MTyr4 (24.9 mg, 0.03 mmol) was
slowly added into the system. The reaction lasted for 1 h in an ice bath
and 24 h at room temperature. After the reaction, THF and DMSO in
the system were removed. The obtained products were purified by
dialysis (molecular weight cut-off = 1,000 Da) against ethanol, and fresh
ethanol was replaced every 12 h. After that, the ethanol was replaced by
deionized water, and deionized water was replaced every 4 h. The final
product was lyophilized for 48 h, yielding a white solid (19.5 mg, yield
60.9%). ^{1}H NMR (500 MHz, DMSO-d_6): δ = 9.35−9.15 (dd, 4H), 8.59 (d,
1H), 8.20 (m, 2H), 7.88 (s, 3H), 7.03 (m, 8H), 6.65 (m, 8H), 5.33 (m, 2H),
4.65−4.15 (m, 8H), 3.05−2.60 (m, 10H), 2.35−1.90 (m, 8H), 1.21 (m, 26H),
0.86 (m, 3H).

Fabrication of MTyr−OA nanomicelles in water

MTyr−OA nanomicelles were prepared according to our previous
work: 2.0 mg MTyr4−OA powder was dissolved in 2 ml THF, and the
solution was slowly added to 8 ml deionized water upon stirring. THF
was then removed by dialysis (MWCO = 7,000 Da) against deionized
water for 48 h and fresh deionized water was replaced every 4 h. The
MTyr−OA nanomicelles (named MTyr−OANP) were concentrated by
an ultrafiltration device. The final concentration of MTyr−OANPs
was 8.0 mg ml^{-1}. Tyr−OA nanomicelles were prepared using the same
method as for MTyr4−OA.

Characterization

The ultraviolet−visible spectra of the samples were measured using
a Shimadzu UV-3600 Plus; data were collected using LabSolutions
ultraviolet−vis 1.12 and analysed using Origin Pro 9.0. ^{1}H NMR spectra
were recorded on an AVANCE AV400 spectrophotometer (AVANCE
III, BRUKER); data were collected using TopSpin 3.2 and analysed
using MestReNova 14. The fluorescence spectra were recorded on a
steady-state and lifetime fluorescence spectrometer (FLS1000, Edin-
burgh); data were collected using Fluoracle V2.5.0 and analysed using
Origin Pro 9.0. Dynamic light scattering and zeta potential measure-
ments were carried out on a Zetasizer Nano analyser (Zetasizer Nano
ZS90, Malvern); data were collected using Zetasizer software (ver-
sion 6.34) and analysed using Origin Pro 9.0. Transmission electron
microscopy (TEM) images were performed on a JEOL JEM-2100F TEM
working at 200 kV and analysed using DigitalMicrograph 3.5. Samples
for TEM were prepared by dropping the nanoparticle solution onto
a carbon-coated copper grid and then dried at room temperature.
The labelling rates of ^{125}I for MTyr−OANPs were measured using a
radio-thin-layer chromatography scanner (B-MS-1000, Eckert & Ziegler

Radiopharma); data were collected using an HW-2000 workstation and
analysed using Origin Pro 9.0. The SPECT images were obtained using
a SPECT/CT scanner (Symbia T16, Siemens), and data were collected
using syngo MI Applications VA60E software. All the measurements
were carried out at room temperature.

Measurement of CMC

Pyrene (5 mg) was dissolved in 100 ml acetone to obtain pyrene solu-
tion (50 μg ml^{-1}). Pyrene solution (5 μl) was added into 10 ml volumetric
flasks and placed in a drying oven at 50 °C for 4 h. Subsequently, differ-
ent concentrations of MTyr4−OA (60 μg ml^{-1}, 30 μg ml^{-1}, 15 μg ml^{-1}, 7.5 μg
ml^{-1}, 3.75 μg ml^{-1}, 1.875 μg ml^{-1} and 0.9375 μg ml^{-1}) were prepared in the
above volumetric flasks and then treated by ultrasonication for 0.5 h.
The fluorescence of MTyr4−OA solution was measured (excitation =
334 nm). The ratio of its fluorescence emission peak at 382 nm to that
at 372 nm was calculated. Lastly, the CMC of MTyr4−OA was calculated
using the fluorescence ratios and sample concentrations.

Tyr release of MTyr−OANPs under peptidase

MTyr−OANPs (5 ml, 2.0 mg ml^{-1}) were placed into a 10 ml glass bottle
at 37 °C with stirring, and 100 μl carboxypeptidase (1,311 units per
ml) was added into the system. A 100 μl sample was taken from the
system at different times (0 h, 1 h, 2 h, 3 h and 4 h) and diluted to 1.0 ml
with methanol, respectively. After all the samples were filtered using
a needle filter (φ13 mm × 0.22 μm, φ represents diameter), they were
analysed by LC-MS. The data were processed using Origin Pro 9.0.

Cell lines and animals

Mouse melanoma cells (B16F10), human skin malignant melanoma
cells (Skmel28, A375, A2058 and Mewo cells), human embryonic kid-
ney cells (HEK-293T), human immortalized keratinocytes (HaCat)
and mouse macrophage-like cells (RAW264.7) were all purchased
from Shanghai Institute of Cells (Chinese Academy of Sciences). Cell
lines were authenticated by morphology and growth characteristics
according to instructions provided on the suppliers' website before
the experiments. B16F10, A2058, Skmel28, HaCat and RAW264.7 cells
were cultured in RPMI 1640 medium (HyClone) supplemented with 10%
fetal bovine serum (HyClone) and 50 IU ml^{-1} penicillin−streptomycin
at 37 °C in a water-jacketed incubator containing 5% wt vol^{-1} CO$_2$.
HEK-293T and A375 cells were cultured in DMEM medium instead. The
mice were housed in an specific pathogen free environment (22 °C with
a 12 h/12 h light/dark cycle, 40−50% humidity) and given free access to
food and water throughout the experiments. All animal experiments
were performed in accordance with the University of Tongji Institu-
tional Animal Care and Use Committee Guidelines (protocol number
TJ-HB-LAC-202305).

Cell viability assay

B16F10, Skmel28, A375, A2058, Mewo, HaCat, HEK-293T and RAW264.7
cells (~2.5 × 10^3 cells per well) were seeded in 96-well plates. After incu-
bation for 24 h, the culture medium of the cells was replaced by fresh
medium containing different concentrations of MTyr−OANPs and
incubated for another 24 h, 48 h or 72 h. Subsequently, for qualitative
assays, the culture media were replaced by calcein-AM/PI staining
solution (100 μl) and then incubated at 37 °C for 30 min. Cell viability
was examined based on cell fluorescence (calcein-AM, Excitation/
Emmision = 494/517 nm; PI, Excitation/Emmision = 535/617 nm) using
an upright fluorescence microscope. Cells with red fluorescence were
recorded as dead cells and cells with green fluorescence were recorded
as live cells, respectively. For quantitative assays, 10 μl CCK-8 solution
was added to each well and incubated at 37 °C for another 2 h. The
absorbance of each well at 450 nm was detected using a microplate
reader (Spark 10M, TECAN) with i-control 2.0 software. Cell viability was
calculated as follows: cell viability (%) = $A_{\text{Cells to be detected}} \times 100/A_{\text{Untreated cells}}$,
where A is the absorbance at 450 nm.

Quantification of melanin

B16F10 cells were seeded in a 6-well plate, and after incubation with MTyr–OANPs (0 mg ml⁻¹, 0.5 mg ml⁻¹ and 1 mg ml⁻¹) for 48 h or 72 h, cells (~1 × 10⁶) were collected and solubilized in 100 μl of 1 M NaOH-10% DMSO at 80 °C for 2 h, and the melanin content was determined by measuring the absorbance at 475 nm using a microplate reader and comparing the results with a standard curve generated obtained with synthetic melanin (Sigma, M8631). For mouse tumours, ~0.1 g of tumour tissue was taken and lysed in 500 μl of 1 M NaOH-10% DMSO at 80 °C for 4 h, and the melanin content was determined using the same method described above. The tyrosinase activity was calculated as the fold change compared with the control.

Tyrosinase activity measurement

For measurement of tyrosinase activity, the L-DOPA oxidation method was used as described previously. Cells were lysed in 50 mM sodium phosphate buffer containing 1% Triton X-100 (Sigma, 93443) and 0.1 mM PMSF (Absin, abs812852) at −80 °C for 30 min, 80 μl of the supernatant and 20 μl L-DOPA (2 mg ml⁻¹) were mixed for 1 h at 37 °C in a 96-well plate, and then the absorbance at 475 nm was measured using the microplate reader. The tyrosinase activity was calculated as the fold change compared with the control.

Cell cycle analysis

B16F10 cells (~5 × 10⁵ cells per well) were seeded in a 6-well plate for 24 h and then the culture medium was replaced with fresh medium containing 0 mg ml⁻¹, 0.5 mg ml⁻¹ or 1 mg ml⁻¹ MTyr–OANPs. After incubation for another 48 h, cells were collected by digesting with trypsin and then fixed with cold ethanol (70%) for 2 h. The cells were stained with PI (Beyotime, C1052) and the fluorescence at 561 nm was detected using an analytical flow cytometer (Beckman Coulter DxFLEX). Data were collected with CytExpert software and the cell cycle distribution was analysed with FlowJo_V10 software.

Quantitative PCR

The cells were lysed, and total RNA were obtained using TRIzol reagent (Life Technologies) and isolated by chloroform, precipitated with isopropanol, washed with 75% ethanol and dissolved in DEPC H₂O. Complementary DNA was synthesized using a cDNA reverse transcriptase kit (Roche) and qPCR was performed using an SYBR green master mix (Roche) and a LightCycler 96 system. Data were collected and analysed with LightCycler 96 SW 1.1 software. Expression results were normalized to *Gapdh* levels, and all qPCR amplifications were performed in triplicates and repeated in three independent experiments. The specific primers are as follows:

Mouse *Tyr*: forward, CTCTGGGCTTAGCAGTAGGC; reverse, GCAAGCTGTGGTAGTCGTCT.
Mouse *Tyrp1*: forward, CCCCTAGCCTATATCTCCCTTTT; reverse, TACCATCGTGGGGATAATGGC.
Mouse *Tyrp2*: forward, TTCTGCTGGGGTTGTCTGGG; reverse, CACAGATGTTGGTTGCCTCG.
Mouse *Mitf*: forward, ACTTTCCCTTATCCCATCCACC; reverse, TGAGATCCAGAGTTGTCGTACA.
Mouse *Hk1*: forward, AACGGCCTCCGTCAAGATG; reverse, GCCGAGATCCAGTGCAATG.
Mouse *Pkm2*: forward, CGCCTGGACATTGACTCTG; reverse, GACTGTACTTGACAATGTTGGGA.
Mouse *Pfkm*: forward, TGTGGTCCGAGTTGGTATCTT; reverse, GCACTTCCAATCACTGTGCC.
Mouse *Gapdh*: forward, TGGATTTGGACGCATTGGTC; reverse, TTTGCACTGGTACGTGTTGAT.
Human *Tyr*: forward, TGCACAGAGAGACGACTCTTG; reverse, GAGCTGATGGTATGCTTTGCTAA.
Human *Tyrp1*: forward, TCTCTGGGCTGTATCTTCTTCC; reverse, GTCTGGGCAACACATACCACT.

Human *Tyrp2*: forward, CTTGGGCTGCAAAATCCTGC; reverse, CAGCACTCCTTGTTCACTAGG.
Human *Mitf*: forward, ATGTTGGATGGGTAGCCAAAG; reverse, TTCGAGAGCGCAAATCTTCTG.
Human *Gapdh*: forward, GGAGCGAGATCCCTCCAAAAT; reverse, GGCTGTTGTCATACTTCTCATGG.

LC-MS/MS analysis

B16F10 cell metabolomics profiling was analysed using an ultra-performance liquid chromatography/electrospray ionization quadrupole time-of-flight mass spectrometry, UPLC/ESI-Q-TOF-MS system (UHPLC, 1290 Infinity LC, Agilent Technologies) coupled to a quadrupole time of flight (AB Sciex TripleTOF 6600). After incubation with MTyr–OANPs (1 mg ml⁻¹) or MTyr–OANPs (1 mg ml⁻¹) + α-arbutin (200 μM) for 72 h, 1 × 10⁷ B16F10 cells were collected for UHPLC-QTOF-MS analysis. B16F10 cells with no treatment were used for data normalization. Blank samples (75% ACN in water) and quality control samples were injected every five samples during acquisition. The data were analysed using Origin Pro 9.0.

Western blotting

Cells were lysed with RIPA buffer supplemented with PMSF. Equal amounts of protein from the cell homogenate were isolated by SDS–PAGE gel and transferred into the nitrocellulose membrane. The membranes were blocked with 5% BSA, incubated with related primary antibody and fluorescent dye-labelled second antibody (Alexa Fluor 790-AffiniPure goat anti-rabbit immunoglobulin G (H + L), JAC-111-655-144, Jackson, 1:10,000) and, finally, the signal was developed using an Odyssey fluorescence scanner (Licor). The images were collected and analysed using ImageStudio Lite 5.2.5. The specific primary antibodies were as follows: P21 (Abcam, ab109199, 1:1,000), cyclin D1 (Abcam, ab40754, 1:1,000), HSP70 (Abcam, ab181606, 1:1,000), HSP90 (Abcam, ab203085, 1:5,000), MMP2 (Abcam, ab92536, 1:2,000), MMP9 (Abcam, ab228402, 1:1,000) and β-actin (Abcam, ab8227, 1:1,000).

Seahorse analysis

B16F10 cells were plated into XF96 plates (102601-100, Agilent) and treated with MTyr–OANPs, MTyr–OANPs + PKM2-IN-1 and MTyr–OANPs + TEPP-46 for 48 h. The experiments were conducted on Agilent Seahorse XF96. ECAR was measured both basally and in response to 25 mM glucose, 1.5 mM oligomycin and 50 mM 2-DG after the baseline measurements. The data were collected and analysed using Wave Controller 2.6 software.

Photothermal conversion under 808 nm laser irradiation

B16F10 cells were seeded in a 96-well plate; after co-incubation with MTyr–OANPs (1 mg ml⁻¹) for 48 h, the cells were irradiated under an 808 nm laser with a power density of 0.28 W cm⁻² for 5 min. During irradiation, the temperature of the 96-well plate was measured using a Ti29 thermal imager (Fluke Corporation) with SmartView IR Analysis and Reporting Software 1.0. The temperature of non-treated cells was also measured as controls. For tumour temperature measurement, B16F10 tumour-bearing mice (20 wild-type 6-week-old C57BL/6 male mice) were intravenously injected with 100 μl of 8 mg ml⁻¹ MTyr–OANPs. Two days post-injection, the tumour was exposed to laser treatment (0.28–0.32 W cm⁻²); the temperature of the tumour was recorded as described above. The tumour of mice injected with PBS was measured as controls. Each experiment was carried out in triplicate.

Tumour targeting, blood half-life and distribution of MTyr–OANPs

For the tumour targeting assay, B16F10 tumour-bearing mice (6 wild-type 7-week-old C57BL/6 male mice) were intravenously injected with 100 μl of 8 mg ml⁻¹ MTyr–OANPs-Cy5.5 or Tyr–OANPs-Cy5.5, respectively. The tumour targeting and distribution of MTyr–OANPs

and Tyr–OANPs were recorded using VISQUE InVivo Smart-LF at 1 h, 3 h, 6 h, 12 h and 24 h. Data were analysed with VISQUE CleVue 1.2 software. For quantitative analysis, 3 wild-type 6-week-old C57BL/6 male mice were intravenously injected with 100 µl ^{125}I-MTyr–OANP and 10 µl of blood was collected from mice tails at different times (3 min, 5 min, 10 min, 15 min, 30 min, 60 min, 120 min, 240 min and 480 min) and kept in a 100 µl Eppendorf tube. The radioactivity intensity of collected blood was recorded using a Gamma Immunoassay Counter (KZ4GC-1200). The data were collected by GC-1200 V4.0 software and results were listed as percent injected dose per gram of blood (%ID g^{-1}), and the blood circulation half-time of MTyr–OANP was calculated according to the fitted curve of radioactivity intensity and blood circulation time. The distribution of ^{125}I-MTyr–OANPs in C57BL/6 mice ($n = 3$, wild-type, 6-week-old, male) was monitored by SPECT at different times (1 h, 2 h and 24 h). Mice were killed 5 h post-injection of ^{125}I-MTyr–OANP, and their major visceral organs (heart, liver, spleen, lung and kidney) and tumours were collected to obtain their SPECT images.

In vivo growth inhibition of cell line-derived xenograft
B16F10 melanoma cells ($1.5 × 10^6$) in 100 µl PBS were injected subcutaneously into the right posterior flanks of wild-type 6-week-old C57BL/6 male mice ($n = 12$). A375 or Mewo melanoma cells ($1.5 × 10^6$) in 100 µl PBS were injected subcutaneously into the right posterior flanks of 6-week-old BALB/c-nude male mice ($n = 12$ for each cell line). When the tumour volume reached ~40 mm^3, the mice were randomly divided into 2 groups, 'PBS' group and 'MTyr–OANPs' group, respectively. In the 'PBS' group, PBS was intravenously injected every 2 days; in the 'MTyr–OANPs' group, MTyr–OANPs (30 mg kg^{-1}) were intravenously injected every 2 days. The tumour morphologies were recorded using an Apple camera, and the tumour size was measured every 3 days for 15 days. The tumour size was calculated using the following formula: tumour volumes (V) = length × width^2/2. On day 6, one of the mouse tumours in each group was resected and fixed in 4% paraformaldehyde solution in PBS at 4 °C for 24 h. After gradient dehydration, the tissues were embedded in paraffin wax and then cut into ultrathin sections (5 µm) for Fontana-Masson staining and immunohistochemistry analysis of Mitf and Ki67, and the bright-field images were taken using a confocal laser scanning microscope (CLSM). When the remaining mice died naturally or the tumour volume reached 2,000 mm^3, survival time was recorded.

In vivo growth inhibition by MTyr–OANPs and 808 nm laser
B16F10 melanoma cells ($1.5 × 10^6$) in 100 µl PBS were injected subcutaneously into the right posterior flanks of wild-type 6-week-old C57BL/6 male mice ($n = 48$). When the tumour volume reached ~40 mm^3, the mice were randomly divided into 8 groups. For the antitumour efficacy of MTyr–OANPs and 808 nm laser ('PBS' group, 'laser only' group, 'MTyr–OANPs' group, 'MTyr–OANPs + laser' group, $n = 5$), respectively. In the 'PBS' group, PBS was intravenously injected every 2 days; in the 'laser' group, the mouse tumours were irradiated by an 808 nm laser (0.28 W cm^{-2}) for 5 min every 3 days; in the 'MTyr–OANPs' group, MTyr–OANPs (30 mg kg^{-1}) were intravenously injected every 2 days; in the 'MTyr–OANPs + laser' group, MTyr–OANPs (30 mg kg^{-1}) were intravenously injected every 2 days and mouse tumours were irradiated by an 808 nm laser (0.28 W cm^{-2}) for 5 min every 3 days. To verify the efficacy of PTT alone ('PBS' group, 'laser (0.32 W cm^{-2})' group, 'MTyr–OANPs' group, 'MTyr–OANPs + laser (0.28 W cm^{-2})' group, $n = 5$), tumours were irradiated with an 808 nm laser (0.32 W cm^{-2}) for 5 min every 3 days. The tumour morphologies were recorded using an Apple camera, and the tumour size was measured every 3 days for 15 days. The tumour volume was calculated using the following formula: tumour volumes (V) = length × width^2/2. On day 6, one of the mouse tumours in each group was resected and fixed in 4% paraformaldehyde solution in PBS at 4 °C for 24 h. After gradient dehydration, the tissues were embedded in paraffin wax and then cut into ultrathin sections (5 µm) using an

ultramicrotome (Leica RM2126RT) for H&E staining and immunohistochemistry analysis of HSP70 and HSP90, and the bright-field images were taken using CLSM. When the remaining mice died naturally or the tumour volume reached 2,000 mm^3, survival time was recorded.

In vivo toxicity assay
Nine healthy male ICR mice (~6 weeks) were randomly divided into three groups ('control group', '1-day group' and '21-day group', $n = 3$), and their body weight was monitored every 2 days. After intravenous injection of 100 µl MTyr–OANPs (100 mg kg^{-1}) for 1 day and 21 days, the major organs (heart, liver, spleen, lung and kidney) and blood of mice in each group were collected for H&E staining and blood biocompatibility test.

Statistical analysis
Quantitative data are presented as mean ± s.d. and analysed by Student's t-test (unpaired, two-tailed) and ordinary one-way analysis of variance (ANOVA) with Tukey's test for multiple comparisons using GraphPad Prism software. The difference in the survival curves was determined by a two-sided log-rank test using GraphPad Prism software. $P < 0.05$ was considered statistically significant.

Reporting summary
Further information on research design is available in the Nature Portfolio Reporting Summary linked to this article.

Data availability
All the data supporting the results are available within the paper and its Supplementary Information. The bulk RNA-seq data and clinical information of patients with SKCM were downloaded from The Cancer Genome Atlas (TCGA) database: https://portal.gdc.cancer.gov/. All raw sequencing data and associated processed data files that support the findings of this study have been deposited in the Gene Expression Omnibus under accession code GSE263497 (https://www.ncbi.nlm.nih.gov/geo/query/acc.cgi?acc=GSE263479). Source data are provided with this paper.

Author contributions
W.B., Y.C., J.W. and D.J. conceived the study. Y.C., C.W. and Y. Wu designed and performed the experiments. C.W., Y. Wang, P.Z. and H.Z. synthesized and characterized MTyr–OANPs. Y.C., Y.M. and F.W. performed cell- and tumour-bearing mice-related experiments. X.J. and J.S. assisted with cell biological and animal experiments. B.Z., H.L., C.W. and Y.C. analysed the data. W.B., Y.C., C.W., J.W., D.J. and Y.Y.C. wrote the paper. All authors interpreted data, discussed results and contributed to the review, revision and finalization of the paper.

Competing interests
The authors declare no competing interests.
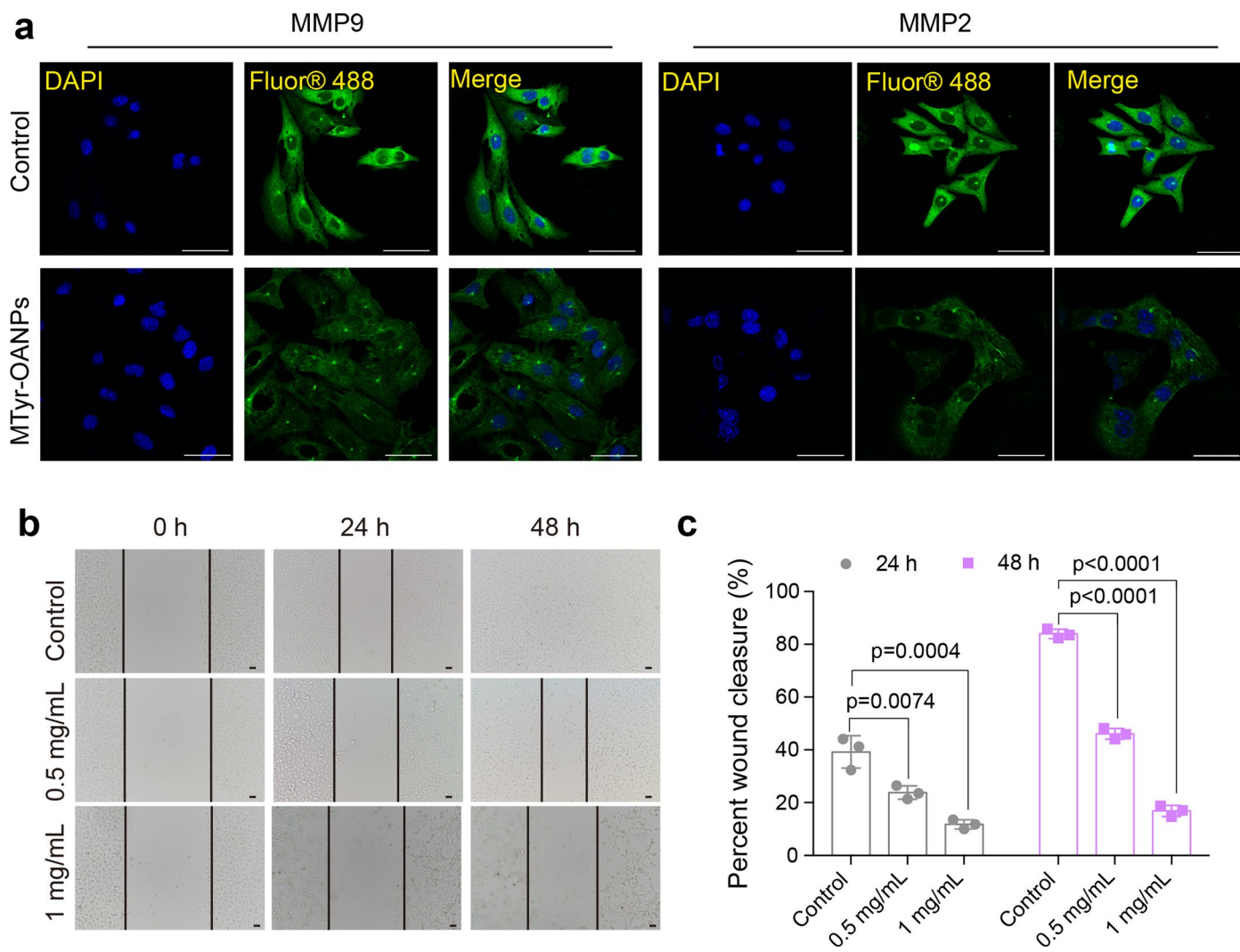
Additional information
Extended data is available for this paper at https://doi.org/10.1038/s41565-024-01690-6.

Extended Data Fig. 1 | MTyr-OANPs downregulated the expression of MMP9 and MMP2, and inhibited cell migration. a, Immunofluorescence images of MMP9 and MMP2 in control and MTyr-OANPs treated cells (n = 3 biological replicates), scale bars, 50 μm. **b** and **c**, wound-healing assay in control and MTyr-OANPs treated cells (n = 3 biological replicates), scale bars, 50 μm. Data were represented as mean ± s.d., and P values were performed with one-way ANOVA followed by post hoc Tukey's test.
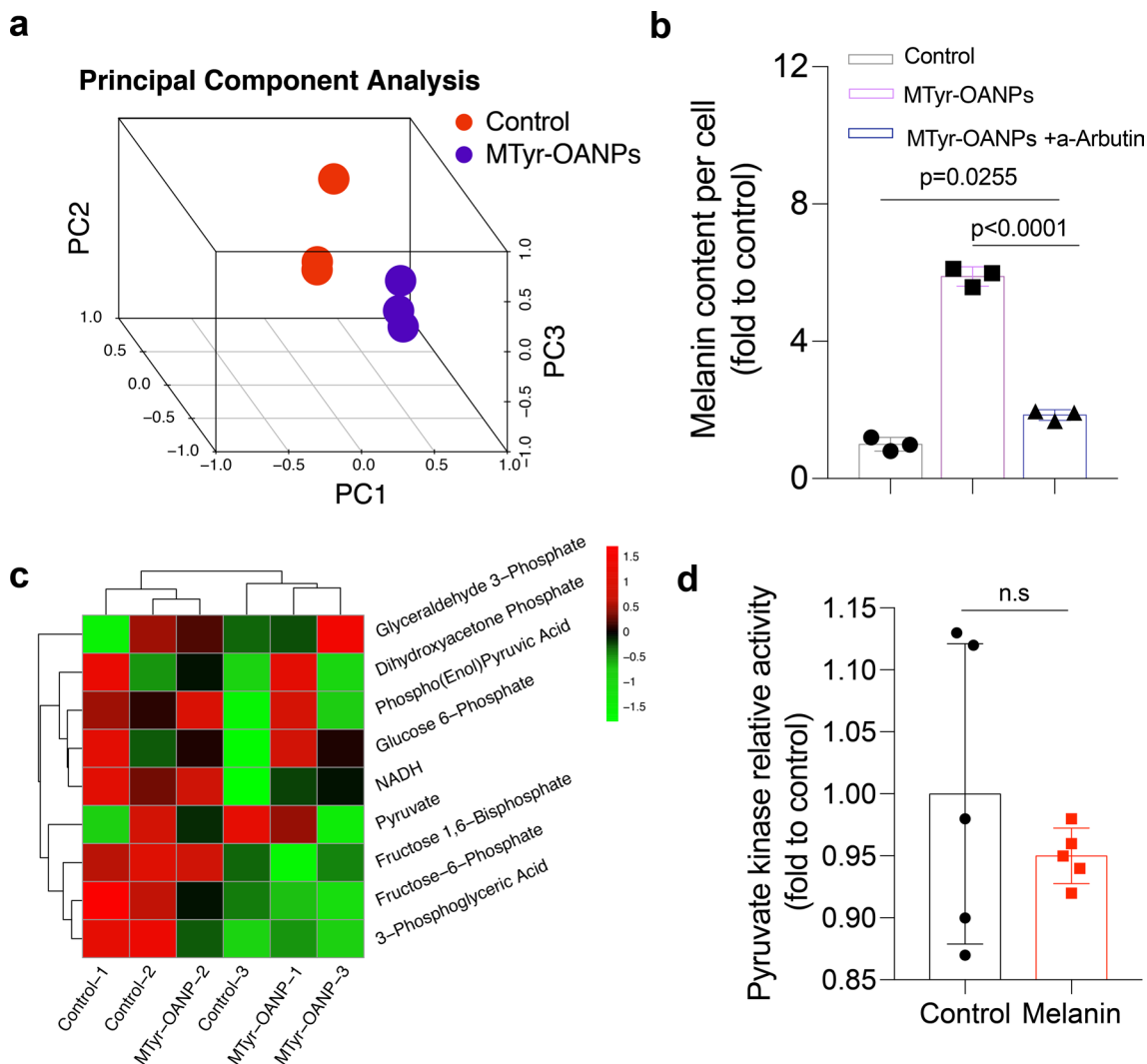
Extended Data Fig. 2 | The metabolite analysis of B16F10 cells after MTyr-OANPs or MTyr-OANPs + α-Arbutin co-treatment. a, Principal Component Analysis (PCA) of metabolites measured by LC-MS in MTyr-OANP (72h after co-incubation) versus control cells (n = 3 biological replicates). **b**, Intracellular melanin content of cell in control, MTyr-OANPs treated, MTyr-OANPs and α-Arbutin co-treated cells after 72h (results were presented as percentage relative to control, n = 3 biological replicates, means ± s.d.). **c**, Heat map of glycolysis intermediate metabolites in MTyr-OANPs and α-Arbutin co-treated cells (72h after co-incubation) (n = 3 biological replicates). Colour bar is Z-score. **d**, Pyruvate activities of B16F10 cells after incubation with melanin for 48 h (p > 0.05, n = 5 biological replicates, means ± s.d.). P values were performed with Student's t test (unpaired, two-tailed) or one-way ANOVA followed by post hoc Tukey's test.

a

b

c
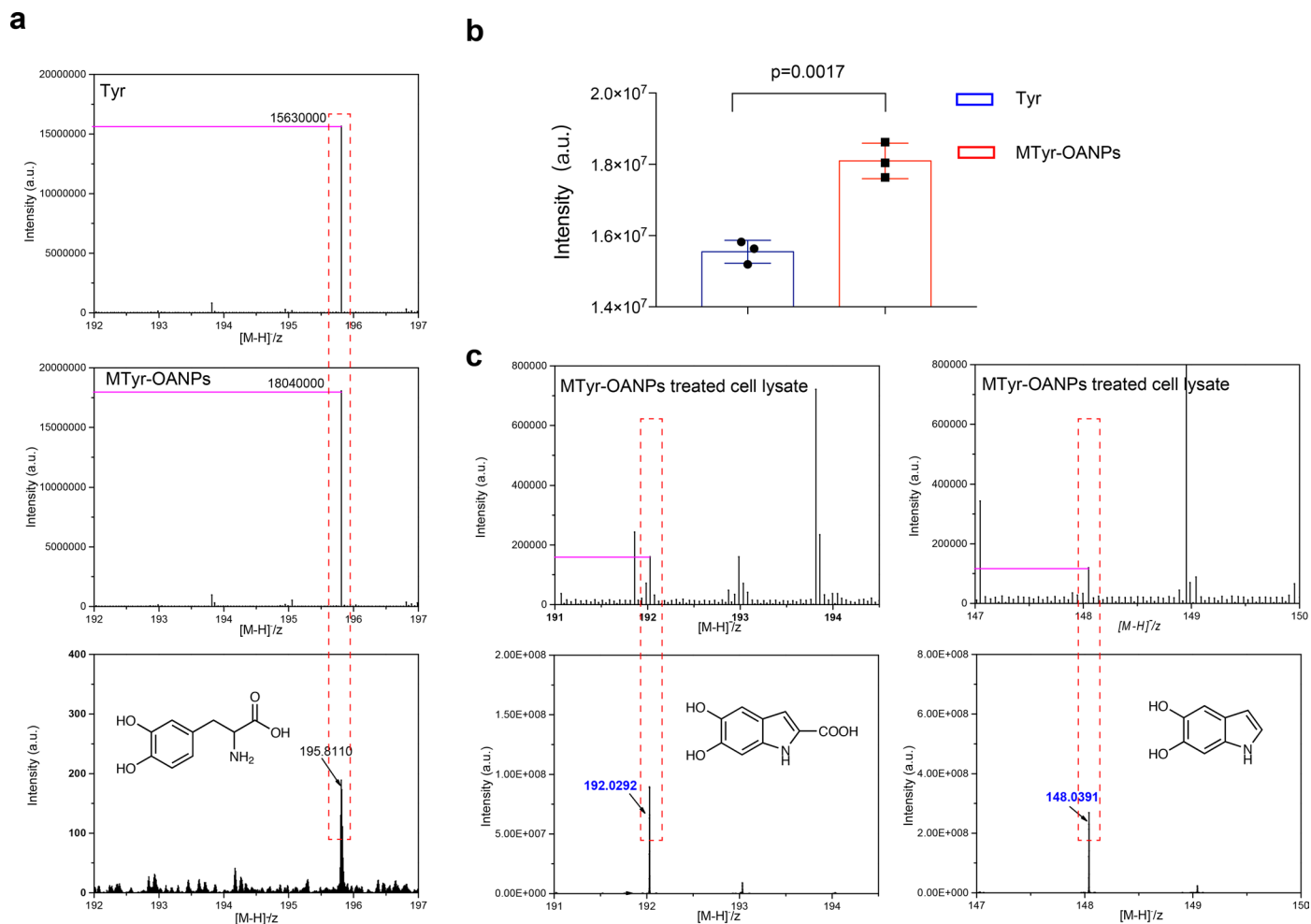
Extended Data Fig. 3 | LC-MS results of melanin intermediates including L-DOPA, 5,6-DHI and 5,6-DHICA after MTyr-OANPs treatment for 72 h. **a**, Mass spectra of intracellular L-DOPA content by LC-MS (n = 3 independent experiments). **b**, Quantitative results based on peak intensity (n = 3 independent experiments, means ± s.d., P value was performed with Student's t test (unpaired, two-tailed). **c**, The mass spectra of DHI and DHICA by LC-MS (n = 3 independent experiments).
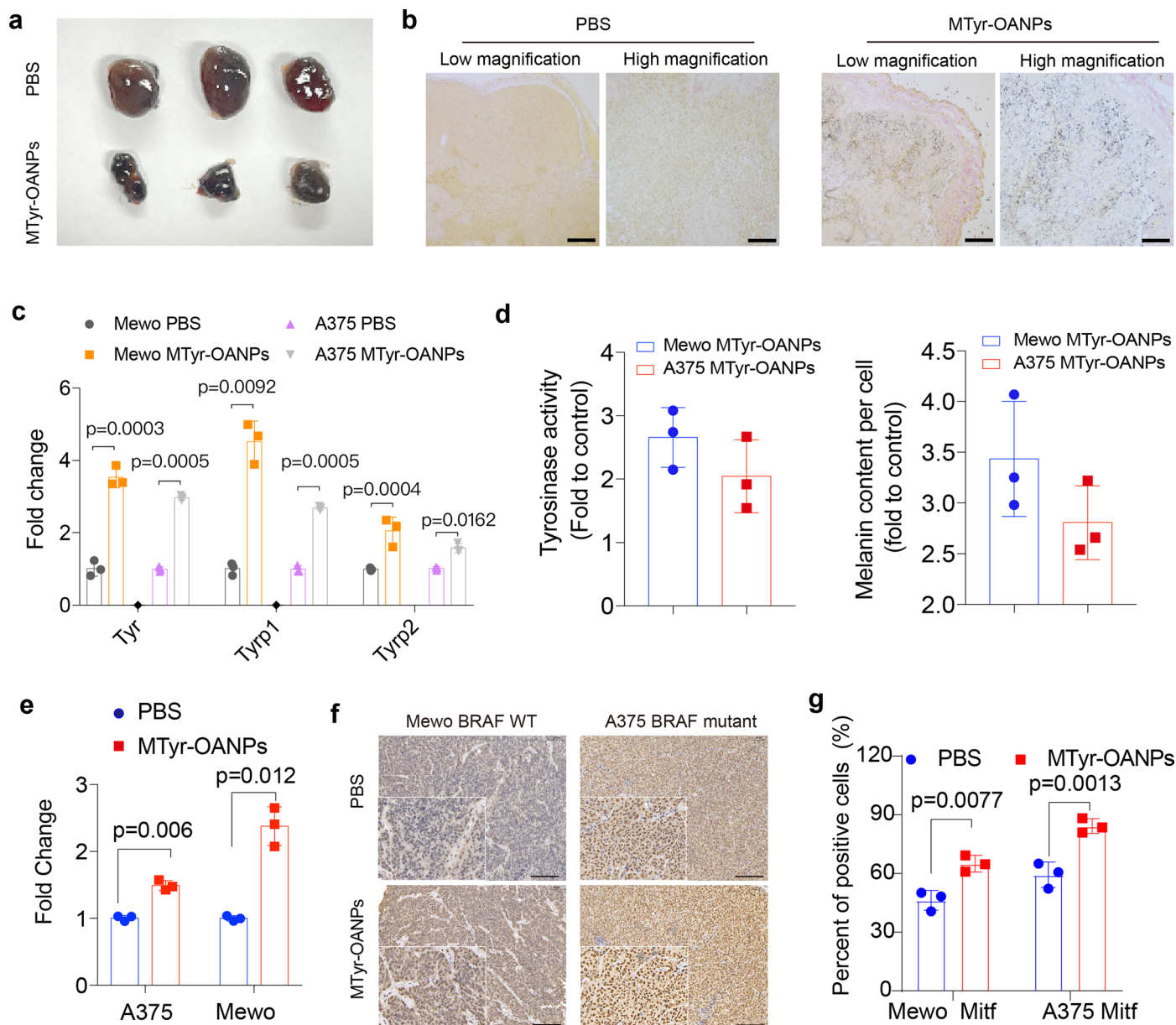
Extended Data Fig. 4 | MTyr-OANPs promote melanin synthesis and related gene expression in murine and human-derived melanoma. Pictures of resected B16F10 tumors (**a**) and Fontana-Masson staining results for melanin of tumor tissue sections (**b**) with or without MTyr-OANPs treatment (n = 3 biological replicates, scale bars, 100 μm). Relative mRNA expression of *Tyr*, *Tyrp1* and *Tyrp2* (**c**), tyrosinase activity and total melanin content (**d**) in PBS and MTyr-OANPs treated mice tumor after three injections (n = 3 biological replicates). **e**, mRNA expression of *Mitf* in A375 and Mewo cells co-cultured with MTyr-OANPs for 24 h. **f** and **g**, Immunohistochemistry results of MITF in mice tumors (n = 3 biological replicates, scale bars, 200 μm). Data were represented as mean ± s.d., and P values were performed with Student's t test (unpaired, two-tailed).
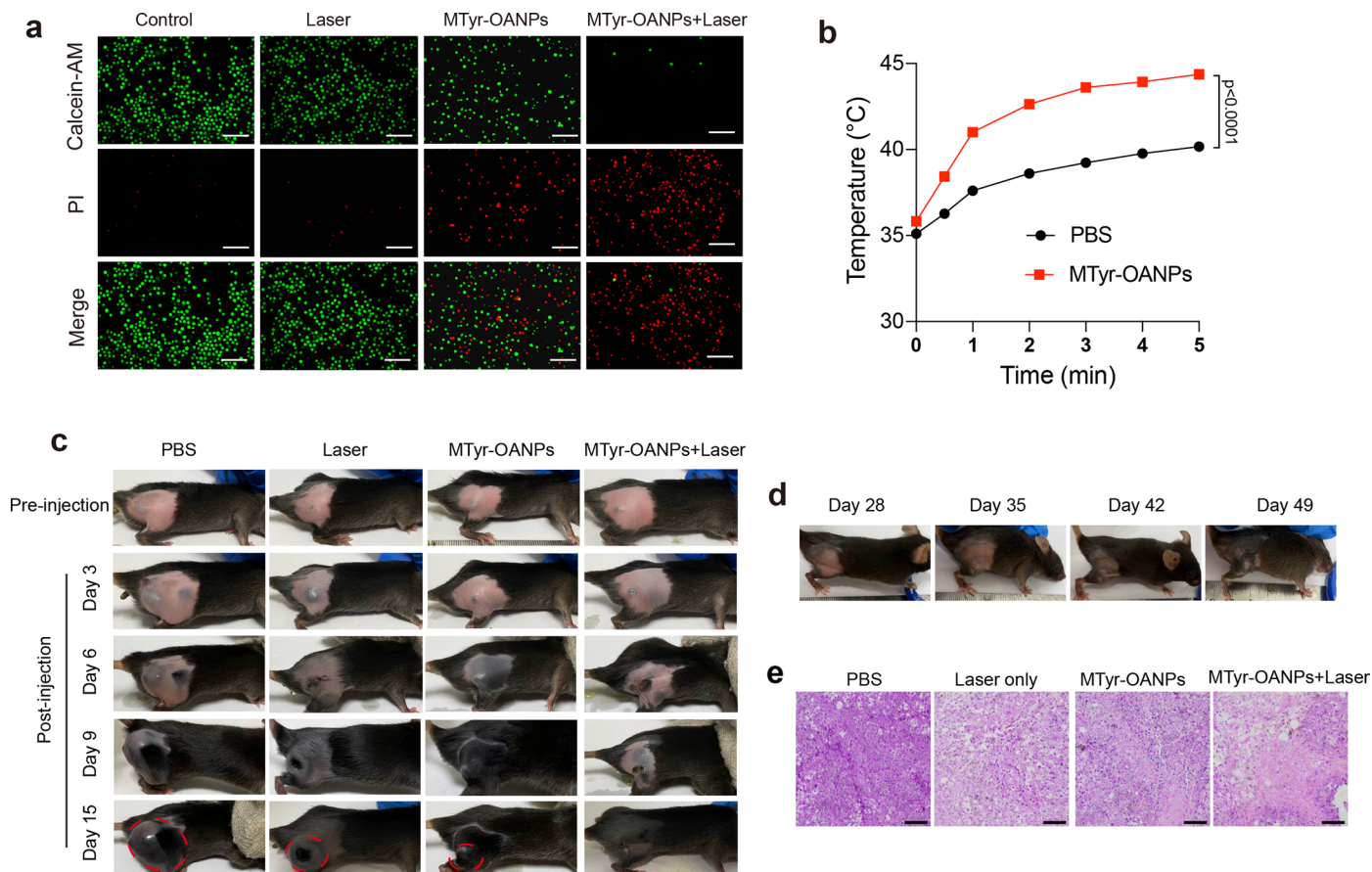
Extended Data Fig. 5 | Enhanced anti-tumor efficiency under MTyr-OANPs and 808 nm laser irradiation co-treatment. a, Fluorescent images of Calcein-AM/PI-stained B16F10 cells incubated with 1 mg/mL MTyr-OANPs for 72 h and/or treated with 808 nm laser for 5 min. (red represents dead cells, and green represents live cells) (n = 3 independent experiments, scale bars, 100 μm). **b**, Temperature increase curves vs. irradiation time of mice tumors (n = 3 biological replicates, means ± s.d. and P values were performed with Student's t test (unpaired, two-tailed)). **c**) Representative images of tumor-bearing mice in different treated groups (n = 5 independent mice). **d**, Representative images of mice in 'MTyr-OANPs + Laser group' within 49 days of observation. **e**, H&E staining of tumors in each groups after 6 days of treatment (n = 5 independent experiments, scale bars, 100 μm).

Extended Data Fig. 6 | The anti-tumor efficiency of photothermal effect after increasing melanin production. Laser power intensity screening to achieve the same photothermal effect as that in 'MTyr-OANPs + Laser' group'. **a**, The tumor temperature increase curves versus irradiation time under different laser power intensity. **b**, Temperature increase curves versus irradiation time in tumors in 'MTyr-OANPs + Laser (0.28 W/cm²)' and 'Laser (0.32 W/cm²)' groups (n = 4 biological replicates, means ± s.d.). **c**, Relative infrared thermal images of mice

(n = 4 biological replicates). Tumor Growth curves (V/V₀) (**d**) and Kaplan–Meimer survival curves (**e**) of B16F10 tumor-bearing mice treated with PBS, MTyr-OANPs, Laser (0.32 W/cm²), and MTyr-OANPs + Laser (0.28 W/cm²), n = 6 biological replicates, means ± s.d. P values were performed with Student's t test (unpaired, two-tailed) or one-way ANOVA followed by post hoc Tukey's test. The differences of survival curves were determined by the two-side log-rank test.

nature portfolio

Corresponding author(s):   Wenbo Bu

Last updated by author(s):   Apr 29, 2024

Reporting Summary

Nature Portfolio wishes to improve the reproducibility of the work that we publish. This form provides structure for consistency and transparency in reporting. For further information on Nature Portfolio policies, see our Editorial Policies and the Editorial Policy Checklist.

Statistics

For all statistical analyses, confirm that the following items are present in the figure legend, table legend, main text, or Methods section.

n/a	Confirmed	
☐	☒	The exact sample size (*n*) for each experimental group/condition, given as a discrete number and unit of measurement
☐	☒	A statement on whether measurements were taken from distinct samples or whether the same sample was measured repeatedly
☐	☒	The statistical test(s) used AND whether they are one- or two-sided *Only common tests should be described solely by name; describe more complex techniques in the Methods section.*
☒	☐	A description of all covariates tested
☐	☒	A description of any assumptions or corrections, such as tests of normality and adjustment for multiple comparisons
☐	☒	A full description of the statistical parameters including central tendency (e.g. means) or other basic estimates (e.g. regression coefficient) AND variation (e.g. standard deviation) or associated estimates of uncertainty (e.g. confidence intervals)
☐	☒	For null hypothesis testing, the test statistic (e.g. *F*, *t*, *r*) with confidence intervals, effect sizes, degrees of freedom and *P* value noted *Give P values as exact values whenever suitable.*
☒	☐	For Bayesian analysis, information on the choice of priors and Markov chain Monte Carlo settings
☒	☐	For hierarchical and complex designs, identification of the appropriate level for tests and full reporting of outcomes
☒	☐	Estimates of effect sizes (e.g. Cohen's *d*, Pearson's *r*), indicating how they were calculated

Our web collection on statistics for biologists contains articles on many of the points above.

Software and code

Policy information about availability of computer code

Data collection	Zetasizer 6.3.4, topspin 3.2, Fluoracle V2.5.0, HW-2000, Fluoracle@,LabSolutions UV-Vis 1.12, syngo MI Applications VA60E, CytExpert 2.4 , NIS-Elements Viewer 4.5, ImageStudio Lite 5.2.5 , Wave Controller 2.6 ,GC-1200 V4.0 software, LightCycler@ 96 SW 1.1 , SmartView® IR Analysis and Reporting Software 1.0,VISQUE CleVueTM 1.2, i-control 2.0,AutoDock Vina 1.1.2, PyMOL 4.3.0,Discovery Studio 4.5.
Data analysis	Origin pro 9.0, GraphPad Prism 8.0.2, ,Flowjo_V10_CL, Wave Controller 2.6 , ImageStudio Lite 5.2.5, DigitalMicrograph 3.5,MestReNova 14.

For manuscripts utilizing custom algorithms or software that are central to the research but not yet described in published literature, software must be made available to editors and reviewers. We strongly encourage code deposition in a community repository (e.g. GitHub). See the Nature Portfolio guidelines for submitting code & software for further information.

Data

Policy information about availability of data

All manuscripts must include a data availability statement. This statement should provide the following information, where applicable:
- Accession codes, unique identifiers, or web links for publicly available datasets
- A description of any restrictions on data availability
- For clinical datasets or third party data, please ensure that the statement adheres to our policy

All the data supporting the results are available within the paper and its Supplementary Information. Source data are provided with this paper. The bulk RNA-Seq data and clinical information of SKCM patients were downloaded from The Cancer Genome Atlas (TCGA) database:https://portal.gdc.cancer.gov/. All raw

Human research participants

Policy information about studies involving human research participants and Sex and Gender in Research.

Reporting on sex and gender	N/A
Population characteristics	N/A
Recruitment	N/A
Ethics oversight	N/A

Note that full information on the approval of the study protocol must also be provided in the manuscript.

Field-specific reporting

Please select the one below that is the best fit for your research. If you are not sure, read the appropriate sections before making your selection.

☒ Life sciences   ☐ Behavioural & social sciences   ☐ Ecological, evolutionary & environmental sciences

For a reference copy of the document with all sections, see nature.com/documents/nr-reporting-summary-flat.pdf

Life sciences study design

All studies must disclose on these points even when the disclosure is negative.

Sample size	Sample sizes were determined on the basis of pre-experiments results analyzed by Student's t test (unpaired, two-tailed) or one-way ANOVA followed by post hoc Tukey's test (type I error [α] = 0.05 and statistical power [1 − β] = 0.8).
Data exclusions	No data were excluded from final analyses.
Replication	All experiments were repeated independently at least three times and the findings were consistent.
Randomization	Randomization was used to divide up the cells and animals for all the in vivo and in vitro study.
Blinding	No blinding was employed since all data reported were objectively measurable data and the researchers performing the treatment were also responsible for the analysis .

Reporting for specific materials, systems and methods

We require information from authors about some types of materials, experimental systems and methods used in many studies. Here, indicate whether each material, system or method listed is relevant to your study. If you are not sure if a list item applies to your research, read the appropriate section before selecting a response.

Materials & experimental systems

n/a	Involved in the study
☐	☒ Antibodies
☐	☒ Eukaryotic cell lines
☒	☐ Palaeontology and archaeology
☐	☒ Animals and other organisms
☒	☐ Clinical data
☒	☐ Dual use research of concern

Methods

n/a	Involved in the study
☒	☐ ChIP-seq
☐	☒ Flow cytometry
☒	☐ MRI-based neuroimaging

Antibodies

Antibodies used	Western-blotting 1. Anti-P21 (Abcam, ab109199, Rabbit monoclonal,1:1000); 2. Anti-Cyclin D1 (Abcam, ab40754, Rabbit monoclonal,1:1000); 3. Anti-HSP70 (Abcam, ab181606, Rabbit monoclonal,1:1000);

4. Anti-HSP90 (Abcam, ab203085, Rabbit monoclonal,1:5000);
5. Anti-β-Actin (Abcam, ab8227, Rabbit monoclonal,1:1000);
6. Anti-MMP2(Abcam,ab92536,Rabbit monoclonal,1:2000);
7. Anti-MMP9(Abcam,ab228402,Rabbit monoclonal,1:1000);
8. Alexa Fluor® 790-AffiniPure IgG (H+L)(Jackson,JAC-111-655-144,Goat Anti-Rabbit Polyclonal, 1;10000).

Validation	1. Anti-P21: https://www.abcam.cn/p21-antibody-epr3993-ab109199.html. 2. Anti-Cyclin D1:https://www.abcam.cn/cyclin-d1-antibody-ep272y-ab40754.html. 3. Anti-HSP70: https://www.abcam.cn/hsp70-antibody-epr16892-ab181606.html. 4. Anti-HSP90: https://www.abcam.cn/hsp90-beta-antibody-epr16621-ab203085.html. 5. Anti-β-Actin:https://www.abcam.cn/beta-actin-antibody-ab8227.html. 6. Anti-MMP2:https://www.abcam.cn/products/primary-antibodies/mmp2-antibody-epr1184-ab92536.html. 7. Anti-MMP9:https://www.abcam.cn/products/primary-antibodies/mmp9-antibody-epr22140-154-ab228402.html. 8. Alexa Fluor® 790-AffiniPure IgG (H+L):https://www.jacksonimmuno.com/catalog/products/111-655-144.

Eukaryotic cell lines

Policy information about cell lines and Sex and Gender in Research

Cell line source(s)	Mouse Melanoma cell line (B16F10), Human skin malignant melanoma cell lines (Skmel28, A375, A2058 and Mewo cells), human embryonic kidney cell (HEK-293T), Human immortalized keratinocytes (HaCat), Mouse macrophage-like cell lines (RAW264.7) were all purchased from Shanghai Institute of cells (Chinese Academy of Science).
Authentication	Cell lines were authenticated by morphology, growth characteristics according to instructions provided on the suppliers' website during the study.
Mycoplasma contamination	All the cells were tested and no mycoplasma contamination were observed.
Commonly misidentified lines (See ICLAC register)	No commonly misidentified cell lines were used.

Animals and other research organisms

Policy information about studies involving animals; ARRIVE guidelines recommended for reporting animal research, and Sex and Gender in Research

Laboratory animals	ICR mice (~ 6 week), BALB/c-Nude (~ 6 week) and C57BL/6 mice(~ 6 week) were purchased from Charles River (CHINA Inc). The mice were housed in a SPF environment (22 °C with a 12h light/dark cycle, 40–50% humidity), and free access to food and water throughout the experiments.
Wild animals	The study did not involve wild animals.
Reporting on sex	Overall 9 of ICR male mice,24 of BALB/c-Nude male mice and 92 of C57BL/6 male mice were used for experiments and since gender does not affect our findings, sex was not considered in study design . Our findings apply to both sexes.
Field-collected samples	The study did not involve samples collected from the field.
Ethics oversight	All animal experiments were performed in accordance with the University of Tongji Institutional Animal Care and Use Committee Guidelines, the protocol number: TJ-HB-LAC-202305.

Note that full information on the approval of the study protocol must also be provided in the manuscript.

Flow Cytometry

Plots

Confirm that:

☒ The axis labels state the marker and fluorochrome used (e.g. CD4-FITC).

☒ The axis scales are clearly visible. Include numbers along axes only for bottom left plot of group (a 'group' is an analysis of identical markers).

☒ All plots are contour plots with outliers or pseudocolor plots.

☒ A numerical value for number of cells or percentage (with statistics) is provided.

Methodology

Sample preparation	For cell cycle analysis, B16F10 cells (~ 5×10^5 cells/well) were seeded in a 6-well plate for 24 h, then the culture medium was replaced with fresh medium containing 0, 0.5 or 1 mg/mL of MTyr-OANPs. After incubation for another 48 h, cells were collected by digesting with trypsin and then fixed with cold ethanol (70%) for 2 h. The cells were stained with PI (Byeotime, C1052) and the fluorescence at 561 nm was detected using an analytical flow cytometer .

Instrument	Beckman Coulter DxFLEX
Software	Data were collected with CytExpert software and analyzed with FlowJo_V10 software.
Cell population abundance	Cells were acquired from the first gate with gate strategy of Forward Scatter Area (FSC-A) and Side Scatter Area (SSC-A) and the second gate strategy of Forward Scatter Area (FSC-A) and Forward Scatter Height (FSC-H), and more than 90% of cells were involved in the following date analysis
Gating strategy	Cell cycle gating strategy: Using Forward Scatter Area (FSC-A) and Side Scatter Area (SSC-A) to find the main group of the cells; Using Forward Scatter Area (FSC-A) and Forward Scatter Height (FSC-H) to remove adherent cell populations; Using Count and PE-A to display the positive cell population for cell cycle analysis, cell cycle was shown in Histogram form.

☒ Tick this box to confirm that a figure exemplifying the gating strategy is provided in the Supplementary Information.